

---

Theses and Dissertations

---

Fall 2012

# Non-invasive stem cell tracking using novel nanomaterials : in vitro and ex vivo studies

Sean Kenneth Sweeney  
*University of Iowa*

Copyright © 2012 Sean Kenneth Sweeney

This thesis is available at Iowa Research Online: <http://ir.uiowa.edu/etd/2282>

---

## Recommended Citation

Sweeney, Sean Kenneth. "Non-invasive stem cell tracking using novel nanomaterials : in vitro and ex vivo studies." MS (Master of Science) thesis, University of Iowa, 2012.  
<http://ir.uiowa.edu/etd/2282>.

---

Follow this and additional works at: <http://ir.uiowa.edu/etd>

 Part of the [Biomedical Engineering and Bioengineering Commons](#)

NON-INVASIVE STEM CELL TRACKING USING NOVEL NANOMATERIALS: IN  
VITRO AND EX VIVO STUDIES

by

Sean Kenneth Sweeney

A thesis submitted in partial fulfillment  
of the requirements for the Master of  
Science degree in Biomedical Engineering  
in the Graduate College of  
The University of Iowa

May 2012

Thesis Supervisor: Adjunct Associate Professor Jose G. Assouline

Graduate College  
The University of Iowa  
Iowa City, Iowa

CERTIFICATE OF APPROVAL

---

MASTER'S THESIS

---

This is to certify that the Master's thesis of

Sean Kenneth Sweeney

has been approved by the Examining Committee  
for the thesis requirement for the Master of Science  
degree in Biomedical Engineering at the May 2012 graduation.

Thesis Committee: \_\_\_\_\_  
Jose G. Assouline, Thesis Supervisor

\_\_\_\_\_  
Tae-Hong Lim, Academic Adviser

\_\_\_\_\_  
Joseph M. Reinhardt

\_\_\_\_\_  
Edwin L. Dove

\_\_\_\_\_  
Eric A. Hoffman

## ACKNOWLEDGMENTS

First and foremost, I must acknowledge the assistance of my research adviser, Prof. Jose Assouline, without which I would not have been able to complete this work. I have also received a great deal of assistance from the undergrads who have worked in Prof. Assouline's lab: Tony Melchiorri, Vijay Permeswaran, and Kevin Townsend. I must also acknowledge Prof. Dan Thedens and the lab of Prof. Robert Weiss, who generously gave their time and expertise for MRI scanning. The lab of Prof. Eric Hoffman gave their time and assisted with fixation of the mouse lungs and CT scanning. In addition, our lab collaborated with the labs of Prof. Victor S.Y. Lin and Prof. Brian Trewyn at Iowa State University, as well as Prof. Markus Winterer, University of Duisburg-Essen to develop novel nanomaterials that are the focus of this research. Finally, I wish to thank my academic adviser, Prof. Tae-Hong Lim, and Professors Joseph Reinhardt and Edwin Dove for serving on my thesis committee.

## ABSTRACT

As research and clinical use of stem cell therapies progresses, it is becoming more evident that being able to visualize the stem cell transplant *in vivo* is of great benefit to the researcher or clinician. As a result, researchers are working to address this need. Our lab is collaborating to develop novel, multimodal nanomaterials, one with a core of mesoporous silica, and the other with a core of gadolinium oxide. Varying modifications have been made as needs arose. Human mesenchymal stem cells (MSCs) were isolated from bone marrow aspirates and confirmed to be positive for STRO-1, a common MSC marker. These cells were labeled with 125  $\mu\text{g/mL}$  of varying nanoparticle types: gadolinium oxide, doped with 0.5%, 5%, or 10% europium for magnetic resonance imaging (MRI) and luminescence microscopy, and mesoporous silica nanoparticles (MSN), loaded with fluorescein for fluorescent microscopy and capped with either iron oxide or gold for MRI and computed tomography (CT), respectively. We studied the kinetics of MSN uptake by MSCs for 10 days using fluorescent microscopy. In *ex vivo* studies, we used the 4.7 Tesla Varian® small animal MRI scanner to detect  $5 \times 10^4$  cells labeled with ferrite-capped MSN particles and injected into the brain, lung, and heart of a perfusion-fixed mouse. Micro-CT was used to detect  $1.7 \times 10^6$  cells labeled with gold-capped MSN and delivered to the lungs via the trachea in a perfusion-fixed mouse. The results of this research are preliminary to *in vivo* testing using animal models as a proof-of-concept for these potentially marketable particles.

## TABLE OF CONTENTS

LIST OF FIGURES .....	vi
CHAPTER	
I. BACKGROUND .....	1
Stem Cell Biology.....	1
Definition.....	1
Sources of Stem Cells; Advantages and Disadvantages of Each .....	1
Embryonic Stem Cells.....	1
Fetal Stem Cells .....	2
Umbilical Cord Blood .....	3
Adult Bone Marrow .....	3
Culture Conditions.....	4
Isolation of Stem Cells by Phenotype .....	4
Nanoparticles .....	6
Mesoporous Silica Nanoparticles .....	6
Other Nanoparticles.....	8
Imaging/Contrast Techniques .....	9
Magnetic Resonance Imaging (MRI) .....	10
X-ray Computed Tomography (CT).....	11
Ultrasound .....	12
Non-invasive Stem Cell Tracking .....	13
Summary .....	17
II. METHODS .....	19
Mesenchymal Stem Cell Culture Characterization.....	19
MSN Particle Characterization, Kinetics of Uptake by Cells.....	20
Imaging/Image Processing.....	21
MRI.....	21
CT .....	23
III. RESULTS .....	25
MSC Culture Characterization .....	25
MSN Particle Characterization, Kinetics.....	26
Imaging/Image Processing.....	28
MRI of Europium-doped Gadolinium Oxide .....	28
MRI of Fe/FITC-MSN-labeled MSCs.....	30
Lung Micro-CT .....	32
IV. DISCUSSION.....	35
MSC Culture Characterization .....	35
MSN Particle Kinetics .....	36

Imaging Studies .....	37
V. CONCLUSIONS .....	41
REFERENCES .....	44

## LIST OF FIGURES

### Figure

1.	TEM images of mesoporous silicate nanoparticles (MSNs). .....	8
2.	STRO-1 labeling of stromal population F015-P1, after 5 days in culture. The primary antibody was obtained from hybridoma cells grown in serum-free CD medium (left) or RPMI/10% serum (right). .....	25
3.	Kinetics of ferrite-capped, FITC-loaded mesoporous silica nanoparticles (MSN) added to human fetal mesenchymal stem cells (A). Pictures were taken at the indicated times following addition of particles to the growth medium at 125 $\mu\text{g}/\text{mL}$ . Scale bars indicate 25 $\mu\text{m}$ . Plots showing healthy proliferation of labeled cells (B), measurement of intracellular MSN particles (C), percentage of particles that are incorporated in cells (D) and percentage of cells that contain at least one detectable endosome of particles (E). Error bars indicate one standard deviation ( $n = 4$ at each data point). .....	27
4.	3-D rendering of the difference subtracted processed MRI of Eppendorf tubes containing the indicated concentrations of nanoparticles suspended in type I collagen. $r_2$ relaxivities calculated using the described method for various concentrations of gadolinium suspended in collagen and scanned at several echo times ( $T_E = 4, 6, 8, 10, 12, 14, 16, 18,$ and $20$ ms). The calculated $T_1$ value was plotted for each nanoparticle concentration and the slope of the best fit line gives the $r_2$ relaxivity ( $3.6 \text{ s}^{-1} \cdot \text{mM}^{-1}$ ). .....	29
5	3D MR rendering of <i>ex vivo</i> mouse brain (A) and lung (C), with injection sites highlighted. Brain was injected with 150,000 labeled hMSCs (right hemisphere, arrow head) and 50,000 labeled hMSCs (left hemisphere, arrow). Lung was injected with 50,000 labeled hMSCs (white arrow). Plots of injection sites' values (in arbitrary MR units) compared with normal tissue (B and D). For both plots, error bars indicate the standard deviation of the volume of interest; statistical comparison of normal tissue to injection site gave a value of $p < 0.05$ . .....	31
6	3D rendering of <i>ex vivo</i> mouse heart into which 3 injections of 50,000 labeled hMSCs were added (A). The three injection sites (indicated by arrows) were manually segmented (volumes of interest shown in ventral view, B, and lateral view, C), and statistical analyses performed (D). .....	32
7	CT of perfusion fixed mouse lung with an intratracheal delivery of $1.7 \cdot 10^6$ cells labeled with gold-capped, FITC-loaded MSN particles. Triplanar 3D view (A) shows region of likely labeling superior to slice indicated by red box. In (B), the slice indicated in (A) shows labeled region (arrow head) and unlabeled region (arrow), used for comparison. Histogram (C) comparing profiles of labeled and unlabeled regions corresponding to those shown in (B), with statistical data tabulated in (D). .....	33

## CHAPTER I. BACKGROUND

### Stem Cell Biology

#### Definition

Stem cells are defined as any cell which can differentiate into more than one type of mature cell. The stem cell potency, or number of cell types arising from a stem cell can vary from the pluripotent cells of the blastocyst of the embryo<sup>1,2</sup> to the epidermal stem cells, whose primary function in nature is simply to replenish sloughed off layers of dead skin<sup>1,3</sup>. In research, stem cells are the perfect tools for tissue engineers; given the proper stimuli, a small population of stem cells can give rise to a large population of mature cells in a manner that mimics the *in vivo* environment. Because of their versatility, stem cells are being aggressively studied as sources of implantable tissue designed to regenerate every type of tissue imaginable. Engineered tissues include commercially available artificial skin<sup>4</sup>, artificial cartilage and bone repair constructs<sup>5-7</sup>, and heart valves<sup>8-10</sup>, as well as the bioartificial liver<sup>11,12</sup>, kidney<sup>13-15</sup>, and pancreas<sup>16,17</sup> in various stages of clinical research. In most cases, the engineered tissues are only used in emergency situations when traditional replacements, such as allogenic transplants, are unavailable.

#### Sources of Stem Cells; Advantages and Disadvantages of

#### Each

#### Embryonic stem cells

In embryology, the fertilized egg (zygote) divides without differentiation until the blastocyst stage, when the embryo is a hollow ball of about 128 cells. At this point, the first differentiation begins, as certain cells will become the embryo itself (the embryoblast), and the remaining cells will become the placenta (trophoblast). Cells of

the embryoblast remain totipotent-that is, any embryoblast cell can form any tissue in the embryo. These are the cells commonly referred to as embryonic stem cells<sup>18</sup>.

As of late 2008, federally funded use of these cells was restricted to a few cell lines developed prior to the legislation<sup>19</sup>. In 2009, the restriction was lifted somewhat, so that federal funding could be requested for research on any cell line already produced. The use of federal funds to produce new embryonic cell lines is still banned, and other aspects of the legislation are in a constant state of flux<sup>20</sup>. In other countries, results of transplants involving embryonic stem cells have been mixed at best. When implanted without proper control measures, these cells can grow into tumors called teratomas<sup>21, 22</sup>, which is one of the primary reasons behind developing *in vivo* tracing methods.

### Fetal Stem Cells

At about 8 weeks' gestation in humans, the developing embryo is reclassified the fetus. At this point, most of the organs are recognizable and functional to some degree<sup>23</sup>. The remaining gestation is primarily for growth, rather than differentiation, of tissues, as the fetus must grow from about 1 inch in length and 8 grams in mass at 8 weeks, to around 20 inches and 3500 grams at birth. Therefore, although the pluripotent cell population may make up a small fraction of the cells of the fetus, most tissues must have a large proportion of multipotent cells-that is, cells that are partially differentiated, but with a great capacity for division (mitosis).

Compared with embryonic stem cells, there are fewer regulations on the utilization of fetal tissues for research. Following elective abortions, these tissues can be donated and are treated in a legal manner similar to the donation of biopsied tissue, provided the investigator is properly credentialed to handle the tissue and no profit is made from the exchange of this tissue<sup>24</sup>.

### Umbilical Cord Blood

The collection of umbilical cord blood after birth as a source of hematopoietic (blood forming) stem cells has been increasing as of late, in part because there is less of an ethical controversy than that of the collection of embryonic or fetal tissue. There is still a debate over whether or not it is beneficial to collect a volume of blood that would ordinarily circulate back into the infant<sup>25</sup>. Several studies have attempted to determine the timing of clamping the umbilical cord for optimal infant safety and cord blood collection<sup>26, 27</sup>. The fact that only hematopoietic cells exist in the cord blood, and in a small percentage of the whole blood, makes this a limited stem cell source for researchers.

### Adult Bone Marrow

With an optimal combination of good potency and freedom from ethical controversy, the bone marrow may be the most ideal of stem cells yet identified. Within the bone marrow exists a population of hematopoietic (blood-forming) stem cells, usually identified by their positive expression of the cell surface marker CD34<sup>28</sup>. The hematopoietic cells interact very closely with a second population of stem cells known as bone marrow stromal cells or mesenchymal stem cells. This population is usually identified by its expression of the marker STRO-1, and has been shown to differentiate into nearly all cells originating from the mesodermal embryonic germ layer, such as adipose, bone, cartilage, and cardiac tissues<sup>29-31</sup>. A more contentious claim is the differentiation of mesenchymal stem cells into neural tissue<sup>32</sup> because neurons have origins in the ectodermal, rather than mesodermal, germ layer<sup>23</sup>. Recently however, a different subset of STRO-1<sup>+</sup> mesenchymal cells of the dental pulp have also been a subject of study for neural differentiation<sup>33</sup>.

The collection of bone marrow from adults is free of the controversy inherent in embryonic and fetal tissue. Typically, a patient donating bone marrow for an allogenic

transplant undergoes a puncture of the iliac pelvic crest. Given consent, a portion of this donation can be retained for research purposes. It has been shown, however, that the potency and yield of these cells declines throughout adulthood.

## Culture Conditions

### Isolation of Stem Cells by Phenotype

It is widely accepted that a subset of cells in the bone marrow stroma act as precursors for osteoblasts and osteoclasts. A more controversial topic is the multipotency of these cells to generate other cell types. Much work has been done, and is currently being done, to further characterize these mesenchymal stem cells. The lab led by Beverly Torok-Storb has identified stromal cell precursors using the monoclonal antibody STRO-1, and has also worked with the University of Iowa's Developmental Studies Hybridoma Bank (DSHB) to develop a hybridoma cell line capable of producing STRO-1 primary antibody for immunohistochemical study<sup>34</sup>. Although it isn't known precisely where in the differentiation spectrum STRO-1<sup>+</sup> cells exist, this cell line appears to be capable of taking on the form of not only osteocytes and fibroblasts in culture, but adipocytes and smooth muscle cells<sup>35,36</sup>. Following this work, many groups have further characterized STRO-1<sup>+</sup> cells<sup>37,38</sup> as well as mesenchymal stem cells with other phenotypic profiles<sup>39-43</sup>. Though the exact phenotypes of the cell lines vary from group to group, all have the common feature of being easily isolated by virtue of their prompt adhesion and proliferation on tissue culture plastic<sup>43</sup>.

By predominately using the flow-activated cell sorter (FACS), STRO-1<sup>+</sup> cells have been tested for their expression of several other commonly used markers. When hematopoietic cells of various phenotypes were tested for binding of STRO-1, it was found that only a subset of CD20<sup>+</sup> cells in the peripheral blood were STRO-1<sup>+</sup>. In the bone marrow, STRO-1 was found to bind cells termed fibroblastoid colony forming units (CFU-F) and to erythroid (red blood cell precursor) cells expressing glycophorin A,

several fibroblastic markers (6.19, TE7, IB10, CD10, CD13, Collagen Type I, II, and III, laminin and alkaline phosphatase), adipocytic markers (6.19 and Oil Red O primarily in pre-adipocytes), and one smooth muscle cell marker (HHF35)<sup>34</sup>. The same group demonstrated in a later study that STRO-1<sup>+</sup> cells are osteogenic as well, citing production of alkaline phosphatase, hydroxyapatite, and osteocalcin<sup>36</sup>. Another study showed that approximately 4% of CD34<sup>+</sup> cells are also STRO-1<sup>+</sup><sup>44</sup>, and more recently, Garcia-Pacheco et al further characterized their STRO-1<sup>+</sup>/CD34<sup>+</sup> cell line isolated by their adhesion to tissue culture plastic over time. This line, termed decidual stromal cells, are also almost completely CD10<sup>+</sup>/CD13<sup>+</sup>, with varying expression of CD21, CD23, CD34, CD80, CD86, HLA-DR, HJ2,  $\alpha$ -smooth muscle actin (ASMA), Alkaline Phosphatase and STRO-1. These cells are also negative for CD14, CD15, and CD45, still more evidence that they are part of the precursor population<sup>45</sup>.

Another group has identified a subset of STRO-1<sup>+</sup> cells that are also CD45<sup>-</sup>/CD49a<sup>+</sup>, and has generated a new antibody, C15, through the infection of E. Coli with Phages containing C15. In addition, the group has sequenced the V<sub>H</sub> and V<sub>L</sub> gene segments of C15<sup>46</sup>. Stewart, et al (2003) used the markers HOP-26 (CD 63), CD49a, and SB-10 (CD166) along with STRO-1 to identify primitive stromal cells, finding that expression of these markers varied among bone marrow specimens and with duration in culture. For example, nearly all CD49<sup>+</sup> cells directly from bone marrow were also STRO-1<sup>+</sup>, but in culture, CD49 was present in both STRO-1<sup>+</sup> and STRO-1<sup>-</sup> subsets. When supplemented with the osteogenesis-promoting steroid dexamethasone (dx), the expression of CD49 increased, both in proportion of cells and in intensity. Treatment with dx was also associated with a decrease in the STRO-1<sup>+</sup>/CD49<sup>-</sup> population. Coexpression of CD63 with the osteogenic marker alkaline phosphatase (AP) was also detected, and increased when supplemented with dx<sup>47</sup>.

If FACS is used to isolate the STRO-1<sup>+</sup> population, it is useful to use negative selection methods. That is, by using a number of antibodies to select and remove all

types of STRO-1<sup>-</sup> cells, the isolated cells will not be laden with the antibodies used for selection. To that end, Galmiche et al isolated a stromal cell line by negative selection using antibodies to CD14, CD33, CD45, and CD68, conjugated to magnetic beads using goat anti mouse IgG. The selected cells were characterized by expression of AMSA, vimentin, vinculin, caldesmon, calponin, and smooth muscle myosin heavy chain (SMMS-1)<sup>48</sup>. A similar method of negative selection was used to isolate stromal cells from murine bone marrow using the markers CD11b, CD34, and CD45. This eliminated virtually all of the hematopoietic cells from the specimen. The isolated cells showed positive expression of Sca-1, CD29, CD44, CD81, CD106, and the stem cell marker nucleostemin, and tested negative for expression of CD11b, CD31, CD34, CD45, CD48, CD90, CD117, CD135, and the transcription factor Oct-4<sup>49</sup>.

In summary, the literature shows that there exist many markers for mesenchymal stem cells from the bone marrow, and to fully characterize each collection, the investigator could examine the expression of most--or even all--of these markers. This strategy would quickly become time- and cost-prohibitive, however, and expression of many of the “minor” markers may vary from specimen to specimen. For the fastest and cheapest screening of specimens, the single most important marker remains STRO-1. For the purposes of our experimentation, we simply identified our cells as STRO-1<sup>+</sup> (see methods).

## Nanoparticles

### Mesoporous Silica Nanoparticles

Up to this point in time, the majority of hMSC experiments have occurred entirely *in vitro*, or in some cases, using nude mice as an *in vivo* model. In the latter cases, cells are typically injected, then immunolabeled upon the sacrifice of the animal, using a subset of the previously described markers. At present, a substantial hurdle is being able to follow the migration and *in situ* differentiation of these cells in the living animal.

Several groups are currently labeling hMSCs with superparamagnetic iron oxide (SPIO) particles in order to enhance contrast for magnetic resonance imaging (MRI), with promising results<sup>50-54</sup>.

In addition to tracking MSCs *in vivo*, it may be beneficial in the case of degenerative diseases to provide the cells with a controlled release of growth factor or other reagent to be released when the cells arrive at the appropriate tissue. As an example, dickkopf-1 (dkk-1) is a Wnt signaling inhibitor that has been shown to regulate the cell cycle of hMSCs<sup>55-57</sup>. In addition, dexamethasone (dx), mentioned above, seems to trigger osteogenic differentiation of hMSCs<sup>47</sup>. A scenario in which hMSCs are kept somewhat dormant, then triggered to proliferate by releasing dkk-1 or dx only when they reach their destination in specific tissue is certainly a promising one.

To that end, the Iowa State University lab of Professors Victor Lin and Brian Trewyn has developed a mesoporous silicate nanoparticle (MSN), a material which combines these ideas and is capable of both *in vivo* detection and drug delivery potential loaded with a reagent of interest by simple diffusion, and capped using SPIOs (figure 1). Once internalized, application of a disulfide-reducing agent, such as dihydrolipoic acid (DHLA) uncaps the particles, allowing the controlled release of the product contained therein. The concept was proven using fluorophore-containing MSNs capped and endocytosed by HeLa cells<sup>58</sup>, followed by cytochrome c<sup>59</sup> as well as vancomycin/ATP taken up by astrocytes<sup>60</sup>.

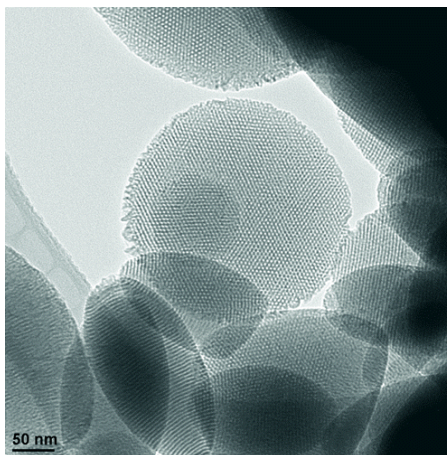


Figure 1. TEM images of mesoporous silicate nanoparticles (MSNs).

Reproduced from Slowing, et al, 2007.<sup>59</sup>

### Other Nanoparticles

While ferromagnetic iron oxide and superparamagnetic iron oxide nanoparticles have been widely used as a clinical magnetic resonance contrast agent for some time, gadolinium compounds have been used more recently. Bayer's Magnevist® and GE's Omniscan® have the majority of the market share, and are gadolinium chelating agents made up of compounds which trap one or more ions of gadolinium within their structure. Recently, recalls over toxicity concerns have arisen with gadolinium MRI contrast agents, in which the chelating molecule releases freely-floating ions of gadolinium into the bloodstream, causing nephrogenic systemic fibrosis (NSF) in rare cases<sup>61, 62</sup>. As a reaction, these agents have been contraindicated in patients with already poor kidney function, while they have been deemed safe for the rest of the population. In the meantime, new forms of chelating agents, such as highly branched dendrimers, are being

designed to have a higher affinity for gadolinium ions, and thus are less likely to release the ions into the bloodstream<sup>63-66</sup>.

In addition, investigators are working on various forms of gadolinium oxide nanoparticles, which in some cases have been shown to have a higher relaxivity than gadolinium chelates, meaning less material can be used for the same level of contrast enhancement<sup>67</sup>. Work has also been done in generating a particle capable of multi-modal imaging using other rare earth elements such as europium<sup>68-70</sup>. These particles have the advantage of being traceable either *in vivo*, using MR, or *ex vivo*, using fluorescent or confocal histology. Europium typically has broad excitation in the ultraviolet (250-350 nm wavelength) spectrum and sharper emission wavelengths at 615 nm. When combined with a development agent can be used in time resolved fluorescence (TRF) assays, or by simply blotting a solution on paper and exposing it to a 254 nm black light<sup>71</sup>. Other groups show similar primary peaks but with several secondary peaks. For example, Goldys et al developed europium-doped Gd<sub>2</sub>O<sub>3</sub> particles and published many spectra, with excitation peaks, from largest to smallest, are 260, 393, 465, 378, 361, and 535 nm, and emission peaks from largest to smallest are 615, 706, 594, 654, and 578 nm. The tallest, sharpest peaks were on particles with the highest europium doping content (content ranged from 0 to 20 mol%)<sup>72</sup>. Based on these spectrophotometry results, we anticipate seeing some signal under the fluorescence microscope when labeling cells and exposing them to a UV light source (approximately 350 nm).

### Imaging/Contrast Techniques

In order to track implanted MSCs *in vivo*, a non-invasive imaging modality is needed. When determining which modality to use, it is important to look at the positive and negative characteristics of each. These include primarily spatial resolution and whether or not the modality produces ionizing radiation in tissue.

## Magnetic Resonance Imaging (MRI)

Magnetic resonance imaging uses small variations in the magnetic field arising from differing proton spin densities  $\rho(x,y)$  in tissue to generate its images. Briefly, the grayscale value at each pixel in a slice of an MR image is the 2-dimensional inverse Fourier transform of that slice's k-space, or frequency domain  $s(t)$ . The radio frequency (RF) data encoded in the frequency domain is collected when small perturbations are made in the larger magnetic field of the MR scanner using smaller gradient coils that vary over time as  $G_x(t)$  and  $G_y(t)$ . The general equations describing the signal are

$$s(t) = \int_{-\infty}^{\infty} \int_{-\infty}^{\infty} \rho(x, y) e^{-j2\pi[k_x(t)x + k_y(t)y]} dx dy,$$

where

$$k_x(t) = \int_0^t \frac{\gamma}{2\pi} G_x(\tau) d\tau, \text{ and}$$

$$k_y(t) = \int_0^t \frac{\gamma}{2\pi} G_y(\tau) d\tau.$$

The MR signal of a specific tissue can also be described by its parameters ( $T_1$ ,  $T_2$ ,  $T_2^*$  relaxation times) and the parameters of the scan (repetition time  $T_R$ , echo time  $T_E$ , and/or flip angle  $\alpha$ ). After a material is magnetized with a certain flip angle  $\alpha$ , the magnetic field in the longitudinal axis  $M_z$  decays (relaxes) with time constant  $T_1$ , and varying the time between pulses (repetition time  $T_R$ ), tissue with different  $T_1$  relaxation times show up with different levels of intensity in the reconstructed image. This is known as a  $T_1$ -weighted image. In a  $T_2$ -weighted image, the echo time  $T_E$  (the time between the pulse and the midpoint of signal readout) is used to generate differing intensities between tissues of different  $T_2/T_2^*$  relaxation times (the time constant of relaxation or “de-phasing” in the transverse plane, or  $M_{xy}$ )<sup>73</sup>.

Besides varying  $T_R/T_E$  on the scanner to achieve the desired contrast, additional contrast can be achieved by using one of several contrast agents. MRI contrast agents are ferromagnetic, paramagnetic, or superparamagnetic materials which interact with the protons present in the surrounding medium, thereby altering the apparent  $T_1$  or  $T_2$

relaxation time. The effect of contrast agents on the observed  $T_1$  or  $T_2$  value is given by the equation

$$\frac{1}{T_{obs}} = \frac{1}{T_{tissue}} + r[contrast],$$

where  $T_{obs}$  is the observed  $T_1$  or  $T_2$  value,  $T_{tissue}$  is the actual  $T_1$  or  $T_2$  relaxation time of the tissue being scanned,  $r$  is the  $r_1$  or  $r_2$  relaxivity of the contrast agent, measured in  $s^{-1} \cdot mM^{-1}$ , and  $[contrast]$  is the molar concentration of the contrast agent<sup>74</sup>.

Of these contrast agents, the most popular are the relatively well-tested ferromagnetic (iron-containing) agents and the somewhat more novel gadolinium agents. Most ferromagnetic contrast agents involve the use of superparamagnetic iron oxide (SPIO), which perturb the tissue's local magnetic field, causing a change in  $T_2$  or  $T_2^*$  relaxation time.

### X-ray Computed Tomography (CT)

Unlike MRI in which the contrast is derived from magnetic properties of tissue, CT images are essentially based on the density of the tissue in the path of the x-rays. In summary, x-ray photons at a known energy are projected towards the patient and detected on the other side. The simplified equation of intensity of the photons striking the detector is given by the relationship

$$I(x) = I_0 e^{-\mu x},$$

where  $I_0$  is the initial intensity and  $\mu$  represents the attenuation coefficient of the material (a function primarily of tissue density)<sup>75</sup>. In order to generate a multislice CT image, this principle is expanded to a 2 dimensional detector which can be rotated around the body. Many 2-D projections are compiled into a 3-D image according to the equation

$$I^{\theta k} = I_0 e^{-\sum_{ij} W_{ij}^{\theta k} \mu_{ij}},$$

where  $I^{\theta k}$  is the intensity data for detector position  $k$  and angle  $\theta$ ,  $w_{ij}$  is a weighting value for position  $(i,j)$  on the detector at position  $k$  and angle  $\theta$ , and  $\mu_{ij}$  is the attenuation of the material at position  $(i,j)$ <sup>75</sup>.

In x-ray CT, contrast agents are effective if they have an ability to greatly change the x-ray opacity of the tissue of interest. Therefore most of the early contrast agents were based on heavy elements such as iodine and barium. Because of toxicity concerns, these agents have evolved over time, and other contrast agents based on electron-dense metals have also been studied, and are well reviewed by Yu/Watson. Of the novel heavy metal contrast agents, those based on gold, bismuth and gadolinium appear to be the most researched thus far<sup>76</sup>.

### Ultrasound

Ultrasound is perhaps the fastest and safest way to obtain *in situ* images, as it requires only a few seconds of preparation with ultrasound gel and produces no ionizing radiation. The drawback is that the spatial resolution does not approach what is possible in CT or MRI at this time. In this modality, a piezoelectric transducer produces sound at high frequencies (typically between 2 and 15 MHz for clinical applications and up to 40 MHz or more for research applications) and generates an image based on the timing of echoes returning to the transducer. Echoes are generated when the propagated sound wave strikes an interface between volumes with differing acoustic impedances ( $Z$ ) and part of the sound wave reflects back to the transducer. Acoustic impedance is defined as  $Z = \rho c$ ,

where  $\rho$  is the density and  $c$  is the speed of sound in the tissue<sup>75</sup>. At the interface between two tissues, the reflectance coefficient ( $R$ ) describes the fraction of sound energy that will be reflected back to the transducer. The remaining fraction continues propagating deeper into the tissue where it may strike another interface.  $R$  is related to

the acoustic impedances of the two tissues at the interface ( $Z_1$  and  $Z_2$ ) according to the equation

$$R = \left[ \frac{Z_1 - Z_2}{Z_1 + Z_2} \right]^2.$$

These principles are applied to the generation of ultrasound images. In A-mode imaging, one transducer is used to plot all the tissue boundaries along one axis as a function of time. One application of A-mode imaging is tracking opening and closing of heart valves or movement of a ventricle during the heart cycle in echocardiography. In B-mode imaging, an array of transducers is coordinated to form a 2-D image. This may be the most common way ultrasound is used, and includes fetal sonography among other applications. Newer ultrasound systems are capable of Doppler mode, in which frequency shifts in the sound wave are used to calculate blood flow through arteries, and even 3-D ultrasound, in which the transducers are swept across many 2-D fields in rapid succession to generate a 3-dimensional image<sup>75</sup>.

#### Non-invasive Stem Cell Tracking

Several groups have previously demonstrated the use of SPIO nanoparticles as a label for certain cells. The consensus methodology appears to be using some form of surface modification or lipofection, a technique normally used for infusion of DNA into cell nuclei, to efficiently get the SPIOs into the cells. *In-vivo* tracking can either be done systemically, by performing an intravenous infusion of labeled cells, or by direct administration into the tissue of interest. The specific methodologies of several papers are reviewed below.

Hoehn et al labeled murine neural embryonic stem cell line HT22 with Sinerem® (AMAG Pharmaceuticals, Inc., Guerbet, France), a form of ultras-small SPIO particles using lipofection techniques. The labeled cells were injected into rat striatum and tracked in a Bruker Biospec® 7 T MRI for up to 16 days. During that time span, the cells were

observed migrating contralaterally, following known pathways in the brain. The authors claim as few as 500 cells could be detected using their system, and that the Sinerem particles remained detectable in the cells for up to 10 generations.<sup>77</sup> Later, the same group labeled mouse embryonic ventricular cardiomyocytes with Sinerem® and injected them into mouse myocardium which had previously been infarcted via coronary artery ligation. They sacrificed the mice and performed ex vivo MRI to simplify image acquisition, and were able to detect the injected cells in this manner. They did not perform in vivo imaging or evaluate whether the injected cells affected any repair of ischemia in the heart prior to the sacrifice of the animals.<sup>78</sup>

Daldrup-Link, et al, compared hematopoietic progenitor cells labeled with 4 different SPIO-derived particles, including 120-180 nm ferumoxides and 20-50 nm ferumoxtran, both dextran-coated iron oxides, 50 nm iron oxide/dextran particles bound to transferrin for receptor mediated endocytosis, and 100-200 nm liposomes loaded with 20-50 nm iron oxide particles coated in an anionic dextran derivative. When loaded into cells and pelleted in a microcentrifuge tube, contrast was strong for all 4 particle types with a variety of scanning parameters (T1- or T2-weighted imaging with either spin-echo or fast-field echo sequences). Compared with the previous paper, the authors used a more clinically applicable 1.5 T MRI scanner, and as a result the threshold for detection of cells was much higher: from  $10^5$  cells for the transferrin-bound iron oxide/dextran particles to  $5 \times 10^5$  cells for the gadopentate dimeglumine particles.<sup>79</sup> In a follow-up, the same group injected  $1 \times 10^7$ ,  $2 \times 10^7$  or  $3 \times 10^7$  ferumoxide-labeled, human CD34<sup>+</sup> hematopoietic stem cells into the tail vein of mice and performed T2\*-weighted MR scans at differing times. Results showed that at 24 hours, many cells were cleared by the liver and spleen, but that some had also arrived at the bone marrow as indicated by a loss of signal (darkening pixels). Histology confirmed that the cells were intact, expressed human CD34, and had retained the contrast agent<sup>80</sup>.

Frank et al similarly labeled human mesenchymal stem cells, mouse lymphocytes, rat oligodendrocyte progenitor cells, and HeLa (human cervical cancer) cells, also using lipofection strategies. They report rates of labeling of nearly 100%, but performed only in vitro MRI scans. MR relaxometry was measured in a 1.0 Tesla scanner on using cell suspensions in gelatin.<sup>50</sup> Bos et al, following the method from Frank et al, labeled rat mesenchymal stem cells using lipofection, and injected cells in rats either in the left renal artery for cell detection in the kidneys, or the hepatic portal vein for tracking in the liver. Relaxometry was measured in a clinical 1.5 Tesla Philips Gyroscan Intera® and showed detectable contrast for up to 12 days following the injection. Histology confirmed engraftment of labeled MSCs in both tissues.<sup>51</sup> As another example of injection directly into tissue, Jendelová et al injected SPIO-labeled bone marrow stem cells or embryonic stem cells of mice into the brains of other mice with brain or spinal cord lesions. Five weeks after the injections, hypointense (dark) regions could be seen at the lesion sites, with the presence of labeled stem cells confirmed by histology<sup>81</sup>. Ko, et al labeled human MSCs with another commercially available SPIO, Feridex®, and cultured them on a gelatin scaffold which was then implanted into an immunodeficient mouse and scanned in a 1.5 T clinical scanner with successful detection.<sup>82</sup>

While iron-based contrast agents have a high  $r_2$  relaxivity ( $100-200 \text{ s}^{-1} \cdot \text{mM}^{-1}$ ), making them useful for  $T_2$ -weighted MRI, they are not as useful for  $T_1$ -weighted imaging. Gadolinium-based contrast agents, on the other hand, have moderate values for both  $r_1$  and  $r_2$ , and can therefore be used for either  $T_1$ - or  $T_2$ -weighted imaging<sup>67</sup>. Contrast agents for MRI based on gadolinium are somewhat newer than those based on iron oxide, but there are still several papers in which investigators used gadolinium to label stem cells for tracking. Hsiao et al used gadolinium-fluorescein MSN particles to label human mesenchymal stem cells, and injected 4000 MSCs into the high brain stem of an immunodeficient mouse. The mouse was scanned on a 1.5 T clinical scanner and the cells were detected for up to 14 days. Unlike the Hoehn paper discussed above, no

migration of the cells was observed.<sup>83</sup> Klasson et al labeled THP-1 cells (a human monocyte cell line from a boy with acute monocytic leukemia) with 2-5 nm diameter gadolinium oxide nanoparticles coated with diethylene glycol. They did not perform any *in vivo* tests, but *in vitro* results confirmed detection of labeled cells in both T1- and T2-weighted MRI, using a 1.5 T clinical scanner.<sup>84</sup> Regino et al used highly branched gadolinium dendrimers (referred to as Gd-G8 dendrimers) for both MRI and CT imaging studies. Unlike most of the previously discussed studies in this summary, the investigators did not label any cells with the particles prior to injection. Rather, they injected particles alone into the right striatum of rats. Using a 3 Tesla GE Signa Excite® clinical scanner, they were able to detect the particles qualitatively, but quantitative measurement of concentration of contrast proved difficult. Computed tomography was performed on a GE LightSpeed Ultra® clinical CT scanner with a source voltage of 140 kVp, with attenuation values comparable to commercially available iodinated contrast agents (6.01 Hounsfield units•mM<sup>-1</sup>).<sup>65</sup>

The use of metallic nanoparticles as a label for tracking cells *in vivo* using CT has not been studied as extensively as MRI; nevertheless, a number of related reports have been published. Similarly to the Regino paper above, Galperin et al have developed radiopaque magnetic nanoparticles with an iron oxide core and iodinated shell for both MR and CT imaging. No *in-vivo* tests were done, but *in-vitro* tests showed positive response in both imaging modalities.<sup>85</sup> Hainfeld, et al first injected mice subcutaneously with carcinoma cells, then followed 10 days later with a tail vein injection of 1.9 nm gold nanoparticles at a concentration of 2.7 mg of gold per gram of mouse weight. Using a mammography scanner, the mice were scanned with a photon energy of 22 kVp for a duration of 0.4 s. The nanoparticles enhanced the contrast in the vasculature, particularly highlighting areas of higher blood flow (the subcutaneous tumors). After 60 minutes, the particles were cleared by the kidneys in an equally efficient manner compared with commercially available iodinated contrast agents<sup>86</sup>. A similar study by Rabin et al

produced equally promising results using 10-40 nm bismuth sulfide nanoparticles<sup>87</sup>. Recently, Cormode et al synthesized high density lipoproteins (HDLs) loaded with 5.6 nm gold nanoparticles and observed uptake by macrophages followed by a significant increase in CT contrast compared with unlabeled cells *in vitro*<sup>88</sup>.

In summary, there is a large body of supporting work for non-invasive in-vivo imaging of stem cells using a variety of contrast agents. In MRI, older methods involve forms of iron oxide, and different methods to cover the surface which helps with cell uptake and cytotoxicity concerns. Earlier papers mostly used lipofection techniques, which are rather intensive compared to the newer papers which used other organic coatings such as dextran. As research progressed from iron oxide to gadolinium particles, the coating of particles was less important since most of the particles were in the form of chelated gadolinium ions. Other forms of gadolinium, such as gadolinium oxide, were coated with diethylene glycol or encapsulated by MSN particles. Once the particles were in the cells, they could be injected intravenously, which leads in most cases to accumulation in the filter organs-liver, kidneys, lungs and spleen, or directly into the tissue of interest which leads to less migration of cells. Both of these methods of administration have advantages and disadvantages depending on the need the investigator is trying to address. The sensitivity of the system is largely dependent on the physics of the scanner; generally and not surprisingly, the investigators using clinical 1, 1.5, or 3 Tesla scanners needed to use more material for detection compared with those who used higher powered research scanners which can approach 12 Tesla. While the majority of CT research is still being done on various forms of iodinated contrast agents, other less toxic heavy metals are being investigated as well-particularly gold, bismuth, and gadolinium. Like the MRI contrast agents, cell toxicity and uptake are improved by using chelating agents or organic shells to reduce exposure of the cell to the heavy metal.

### Summary

Based on the background information presented above, we have collaborated with 2 labs to produce novel nanoparticles according to the following design criteria:

1. The particles must be readily taken up by human mesenchymal stem cells without affecting the cells' ability to divide or differentiate.
2. The particles should be seen *in-vivo* through one or more of the above imaging modalities (MRI, CT, ultrasound, and fluorescence microscopy).
3. The particles may be non-specific now, but should be able to be functionalized in the future to make them more customizable for specific cell applications.

As discussed above, we are working with the Lin/Trewyn lab at Iowa State to develop mesoporous silica nanoparticles. Although they have previously published works involving primarily fluorescence microscopy and commercially available cell lines, we contributed stem cell biology and multimodal imaging findings to help develop even more versatile particles. In addition, we have collaborated with the lab of Professor Markus Winterer of the University of Duisberg-Essen in Essen, Germany, to develop novel nanoparticles of gadolinium oxide doped with europium, which emits light in the visible spectrum when excited by ultraviolet (350 nm wavelength) light. This feature eliminates the need for organic fluorophores such as fluorescein and rhodamine, which are subject to photobleaching.

## CHAPTER II. METHODS

The purpose of this research is ultimately to establish methods for *in vivo* tracking of engineered mesenchymal stem cells (MSCs). This paper focuses on the preliminary work which must be done prior to *in vivo* experimentation, and includes characterization of our isolated MSC population, followed by introduction of contrast media and finally testing in *ex vivo* perfusion-fixed organs using the mouse model.

### Mesenchymal Stem Cell Culture Characterization

Following methods described in the literature<sup>89</sup>, human fetal MSCs were isolated by flushing the bone marrow from 16- to 20-week-old abortuses. The long bones were dissected and transported from the clinic to the lab in 15 mL tubes containing Dulbecco's Modified Eagle Medium (DMEM, GIBCO) with 10% heat inactivated fetal bovine serum (fbs, GIBCO). Within an hour of dissection the articular cartilage and periosteum were removed, and the outer bone surface was cleaned by swabbing with Kimwipes® soaked in 70% ethanol. The bone marrow was flushed using a syringe filled with DMEM/10% fbs and a 22 gauge needle, and the cell suspension was divided evenly among 3-60 mm dishes, one of which contained 5 poly-l-lysine-treated 12mm round glass coverslips.

After 48 hours of incubation, the non-adherent cells were gently rinsed away by repeated pipetting of the culture medium which was then centrifuged. The adherent cells that remained were given 2 mL fresh DMEM along with 2 mL of the centrifuge supernatant (conditioned media). The non-adherent cells were resuspended in 4 mL of the remaining conditioned medium and moved to a 25 cm<sup>2</sup> tissue culture flask.

An immunolabeling of STRO-1 was also performed on two of the coverslips from the same culture according to standard protocols. Briefly, the coverslips were fixed in a solution of 95% ethanol/5% glacial acetic acid for 5 minutes and rinsed in phosphate buffered saline (PBS, GIBCO). Hybridoma-produced mouse anti human STRO-1 monoclonal antibody (Developmental Studies Hybridoma Bank, University of Iowa) was

used at full concentration, and 50  $\mu\text{L}$  was placed on the cells of the coverslip. These were left to react at room temperature for 30 minutes and rinsed with PBS. Next, 50  $\mu\text{L}$  of a 1:50 dilution of goat anti-mouse IgM/FITC was added as the secondary antibody, reacted for 30 more minutes, and rinsed again. The coverslips were mounted on a microscope slide and exposed to 494 nm light. The pattern of STRO-1 labeling was compared with previous studies already published<sup>34</sup>.

#### MSN Particle Characterization, Kinetics of Uptake by Cells

Uncapped MSNs containing covalently bound fluorescein (FITC-MSN) as well as MSNs loaded with FITC and capped with SPIOs (Fe-MSN) were generously provided by Professor Victor S.Y. Lin (Iowa State University). Gadolinium oxide nanoparticles with varying levels of europium doping (0.5%, 5%, 10%) were provided by Professor Markus Winterer (Universität Duisberg-Essen, Essen, Germany). A stock solution of each species of nanoparticle was created by suspending the particle in 500  $\mu\text{L}$  PBS. The suspensions were immersed in a sonicating water bath for 30 minutes and a series of dilutions from 10-500  $\mu\text{g}/\text{mL}$  were added to 25,000 cells in a 24 well plate. After up to a week of incubation, the optimal dose that did not cause excessive cell death was found to be 125  $\mu\text{g}/\text{mL}$ . This was the case for each type of nanoparticle; from that point forward, this was the dosage most commonly used. To study uptake over time, 100  $\mu\text{g}$  MSNs were added to each of the wells of mesenchymal stem cells seeded previously. To view uptake of the particles, the 6 well plate containing FITC-MSN particles was imaged using the Olympus® IX70 fluorescence microscope with green 494 nm filter and with an attached DP70 digital camera and software. Images were obtained at 1 hour, 6 hours, and 26 hours following addition of the particles. After 27 hours, particles that were not engulfed were rinsed from the culture using D-PBS, and more images taken on subsequent days.

Image analysis was done using a MATLAB® program. Briefly, the images were normalized to use the entire range of green pixel values from 0-255 with no saturation, then the built-in MATLAB® edge detection function was used to isolate single cells. The extracellular area was masked out, and bright green pixels within cells above a user-defined threshold were counted, and these numbers were used to estimate the volume of MSN particles internalized over time.

### Imaging/Image Processing

#### MRI

For the europium-doped gadolinium oxide particles, Eight 500  $\mu\text{L}$  Eppendorf tubes were filled with 300  $\mu\text{L}$  of varying concentrations of nanoparticles (1 % Eu-Gd<sub>2</sub>O<sub>3</sub>: 150 and 500  $\mu\text{g}/\text{mL}$ ; 0.5% Eu-Gd<sub>2</sub>O<sub>3</sub>: 50, 150 and 500  $\mu\text{g}/\text{mL}$ ) and suspended in a highly viscous suspension of type I collagen derived from rat tail tendon. This would prevent formation of a pellet during the MRI scan. In addition, a tube containing collagen only was added as a negative control. The tubes were placed in the 4.7 Tesla Varian® MR scanner and scanned to determine the  $r_2$  relaxivity through a sequence of T<sub>2</sub>-weighted scans (relaxation time T<sub>R</sub>=35 ms, echo time T<sub>E</sub>= 4, 6, 8, 10, 12, 14, 16, 18, and 20 ms). In addition, pairs of T<sub>2</sub>\* gradient echo scans (T<sub>R</sub>=35 ms and T<sub>E</sub>=6 and 14 ms, 256 slices and a voxel size of 148  $\mu\text{m}$  per side) were performed.

To calculate the  $r_2$  relaxivity of the gadolinium oxide particles, the program “MRI Analysis Calculator” was downloaded from the ImageJ website (<http://rsbweb.nih.gov/ij/plugins/mri-analysis.html>). This program requires as input an image stack containing the same slice of data at each of the different echo times. It then calculates the T<sub>2</sub> value at each pixel in the slice using a Simplex best-fit algorithm to solve the following equation for T<sub>2</sub>:

$$S_n = S_0 e^{(-T_{E_n}/T_2)},$$

where  $S_n$  is the signal value at the pixel at each echo time  $T_{En}$  and  $S_0$  is the initial magnetic field (a constant)<sup>89, 90</sup>.

After obtaining the  $T_2^*$ -weighted scans, post-processing was done in both ImageJ and MIPAV. In ImageJ, the images from the 2 different scans were subtracted, and the difference saved as a third image. This difference image was also put through the automated background subtraction algorithm in ImageJ, with a radius of 50 pixels, to smooth the background noise. In MIPAV, volumes of interest (VOIs) of each of the tubes in both the  $T_E=6\text{ms}$  and the difference image were selected by manual segmentation. Additional VOIs were selected for PBS controls. VOI volumes and average MR intensities were obtained and saved to a separate file for further analysis.

For MRI using MSN particles, cells were prepared according to the above protocols for isolation and labeling, this time using nanoparticle capped (iron oxide, gold, or bismuth), FITC-loaded MSN particles (Fe/FITC-MSN, Au/FITC-MSN and Bi/FITC-MSN) at a concentration of 125  $\mu\text{g/mL}$  in the growth media. One day after labeling and immediately prior to the experiments, the cells were loosened from the surface of their culture dish using TRYPLEexpress® (GIBCO), suspended in a small volume of phosphate buffered saline (PBS, GIBCO), sampled and counted using Trypan Blue exclusion dye and a hemacytometer. A mouse was then given an intraperitoneal injection of 0.1 mL heparin and anesthetized in a chamber of isoflurane until non-responsive to paw pinching with forceps.

For *ex vivo* MR imaging, the chest cavity was opened and the inferior vena cava (IVC) was severed. A gravity-fed apparatus containing normal saline with a 22 gauge needle was inserted into the right ventricle of the mouse to clear the blood from the vasculature. Both fluids were set on a shelf approximately 1.5 meters above the benchtop in order to deliver the fluids at a hydrostatic pressure of about 110 mmHg, or roughly the systolic pressure of a normal mouse. After the blood draining from the IVC ran clear, the apparatus was switched to deliver 4% paraformaldehyde. Perfusion fixation was

continued until the mouse's tail curled and then went straight, a sign of muscle fibers cross linking (about 10 minutes of flow). Injections of quantities of Fe/FITC-MSN labeled cells were made into the tissues as noted, as were PBS sham injections and needle sticks only as controls. T2\*-weighted pulse echo sequences were used for MR imaging.

## CT

For micro-CT imaging, a similar method was used; however, prior to opening the chest cavity, the trachea was exposed, partially cut, and cannulated with a flexible 22 gauge Luer-lok cannula. Through the cannula,  $1.7 \times 10^6$  cells labeled with Au/FITC-MSN were delivered to one of the lungs. The lungs were then inflated by connecting the cannula to a source of air pressure for the remainder of the perfusion fixation. The heart/lungs were dissected out as one unit, still under air pressure through the trachea, and dried in a drying oven for several days. Scans were performed at varying voltages and currents.

For both CT and MRI, the freeware medical image processing program MIPAV was used for image analysis. The isolevel selection tool was used to manually segment volumes of interest (VOIs): in MR heart imaging, the injection sites as well as control volumes for myocardium and paraformaldehyde, and in CT lung imaging, the terminal bronchioles containing labeled cells as well as an unlabeled region in the contralateral lung. For each VOI, MIPAV calculated the mean and standard deviation of intensity value and number of voxels, and these figures were used for pairwise statistical analysis using the t-test for comparison of two means with independent samples and unequal variances:

$$t = \frac{(\bar{x}_1 - \bar{x}_2) - (\mu_1 - \mu_2)}{\sqrt{(s_1^2/n_1) + (s_2^2/n_2)}}; \nu = \frac{\left[ \frac{s_1^2}{n_1} + \frac{s_2^2}{n_2} \right]^2}{\left[ \frac{(s_1^2/n_1)^2}{n_1 - 1} + \frac{(s_2^2/n_2)^2}{n_2 - 1} \right]}$$

where  $n_1$  and  $n_2$  are the number of voxels in each VOI,  $s_1^2$  and  $s_2^2$  are their respective standard deviations,  $\bar{x}_1$  and  $\bar{x}_2$  are their means and  $v$  is the degrees of freedom used in reference to the statistical lookup table.

## CHAPTER III. RESULTS

### MSC Culture Characterization

Figure 2 shows two typical examples of the labeling pattern of STRO-1 on human mesenchymal stem cells isolated from bone marrow aspirates. The hybridoma cells which produce the STRO-1 antibody were grown in either serum-free CD medium or RPMI+10% fetal calf serum. The choice of growth medium can alter the antibody's quality, so both were tested. Both examples show a pattern of perinuclear, punctiform labeling, typical of patterns previously shown<sup>34</sup>. This shows that both primary antibodies are viable at their present concentration, and that the STRO-1 protein is present in fetal bone marrow at 5 days in culture.

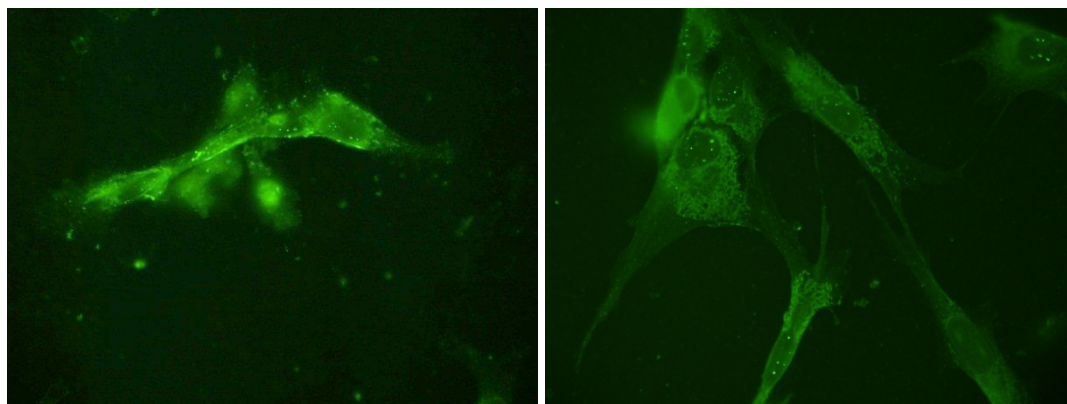


Figure 2. STRO-1 labeling of stromal population F015-P1, after 5 days in culture. The primary antibody was obtained from hybridoma cells grown in serum-free CD medium (left) or RPMI/10% serum (right).

In addition, there appears to be a small amount of excessive fluorescent signal of the antibody grown in serum-free CD medium, which can be seen in the figure as larger clusters of signal inside and outside of the cells. These artifacts do not follow the pattern

seen in previously published results, and are likely caused by non-specific binding of antibody, something that occurs when serum is not present to block it. In future experiments, the antibody grown in RPMI + 10% serum will be preferable to serum-free CD medium for this reason.

#### MSN Particle Characterization, Kinetics

As shown in figure 3, early binding of FITC-MSN particles to cell membranes is observed after one hour, with further binding and early endocytosis by 7 hours. At 26 hours, most of the particles appeared to be in the outer regions of cell cytoplasm, and few particles remained outside the cells. Nevertheless, the cells were rinsed and photographed at 27 hours to confirm that the particles were indeed inside the cells, rather than settled loosely on top of them. As the days progressed, the particles were seen to homogenize into fewer, larger compartments and migrate towards the cell nuclei, likely indicating that they are being compartmentalized into vesicles. A few dividing cells were observed throughout the experiment, showing the equal cytoplasmic division of particles between daughter cells. The same patterns of internalization, compartmentalization and division appeared with the Fe-MSN particles. It was also observed in these cells, however, that cells that took up a disproportionately large amount of particles were found to be apoptotic. Sonicating the particles to ensure the particle dispersion was as uniform as possible helped to prevent this overdosing of some cells. Following the growth curve shown (figure 3B), the cells grew in a manner similar to unlabeled cells, doubling in number about every 3 to 4 days until reaching contact inhibition in about 10 days.

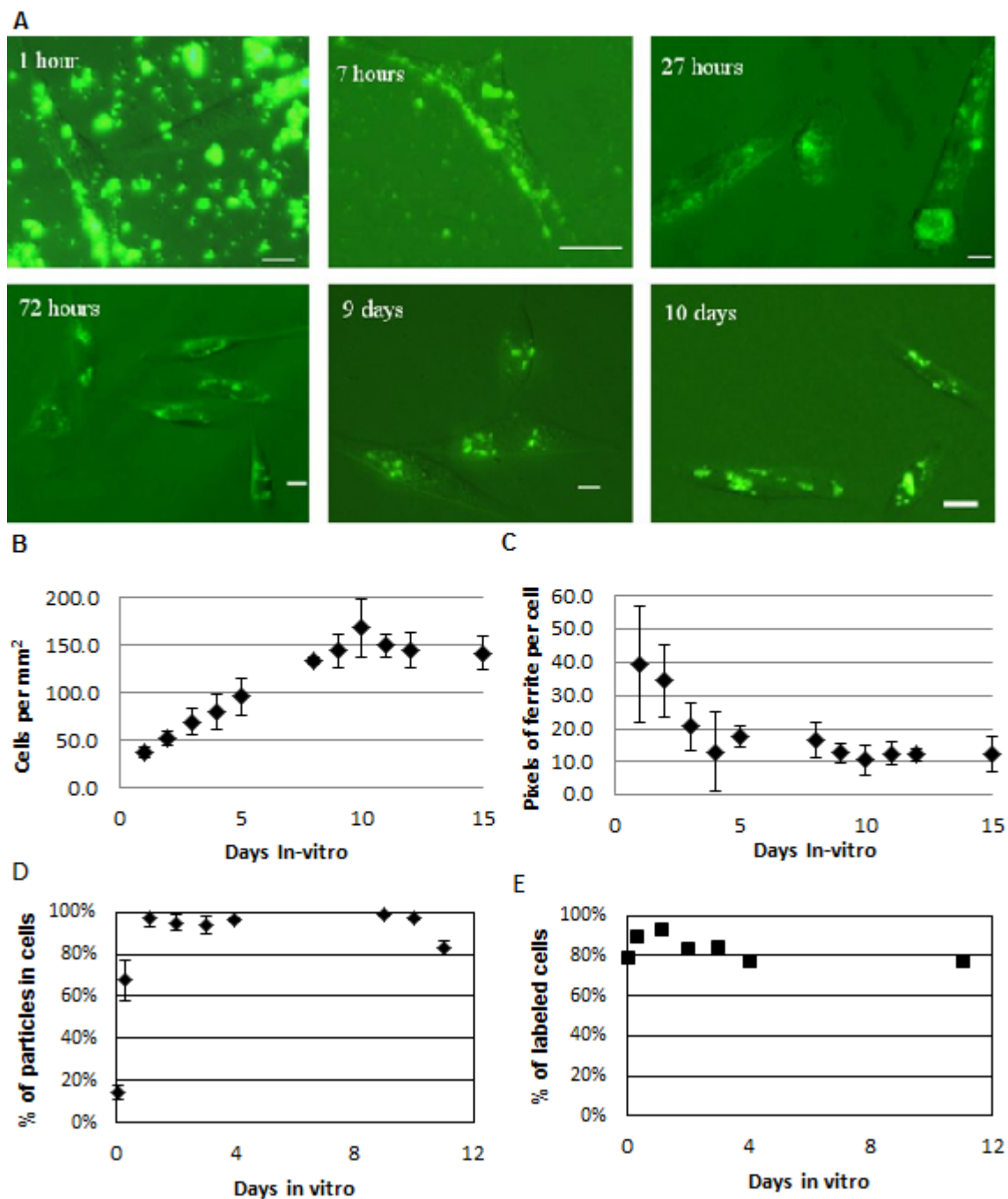


Figure 3. Kinetics of ferrite-capped, FITC-loaded mesoporous silica nanoparticles (MSN) added to human fetal mesenchymal stem cells (A). Pictures were taken at the indicated times following addition of particles to the growth medium at 125  $\mu\text{g}/\text{mL}$ . Scale bars indicate 25  $\mu\text{m}$ . Plots showing healthy proliferation of labeled cells (B), measurement of intracellular MSN particles (C), percentage of particles that are incorporated in cells (D) and percentage of cells that contain at least one detectable endosome of particles (E). Error bars indicate one standard deviation ( $n = 4$  at each data point).

An image processing algorithm of edge detection and digital masking was implemented using MATLAB to automatically segment the cells. Next, a threshold was set so that only MSN particles (by far the brightest green objects in the images) were made positive. This procedure allowed us to count the percentage of labeled cells, the percentage of particles inside cells versus outside cells, and the number of particle-containing pixels per cell (figure 3, B-E). As expected, nearly all the particles remained in cells after the first day, and throughout the observation, 80-90% of the cells were labeled at any given time. This is further evidence that the MSN particles do not interfere with growth; if unlabeled cells grew faster than labeled ones, the percentage of labeled cells would diminish over time. In addition, the number, size, and intensity of vesicles containing particles agree with the observation that during mitosis, each daughter cell tends to receive half of the particles.

### Imaging/Image Processing

#### MRI of Europium-Doped Gadolinium Oxide

In a previous MRI experiment attempting to scan the particles suspended in phosphate buffered saline, it was observed that the particles settled too much before and during the scan. To overcome these effects, a highly viscous, concentrated solution of type I collagen derived from rat tail tendon was made into which various concentrations of nanoparticles could be suspended with less settling. Results are summarized (figure 4), and it can be seen that there are some slight non-homogeneities within the tube; darker areas near the top of the tube suggest lower nanoparticle concentration, while higher intensities at the bottom of the tube suggest higher concentrations. The standard deviations of the average intensities, when measuring the entire volume of the tube, was similar to those of other scans, so it was deemed that the dispersion was maintained reasonably well for the duration of the scan. When the difference-subtracted images were normalized to collagen and measurements made, the resulting plots reflected the scans.

The signal intensity in europium-doped gadolinium was about 30% higher than collagen at 50  $\mu\text{g/mL}$ , and increased to about 50% higher at 500  $\mu\text{g/mL}$ .

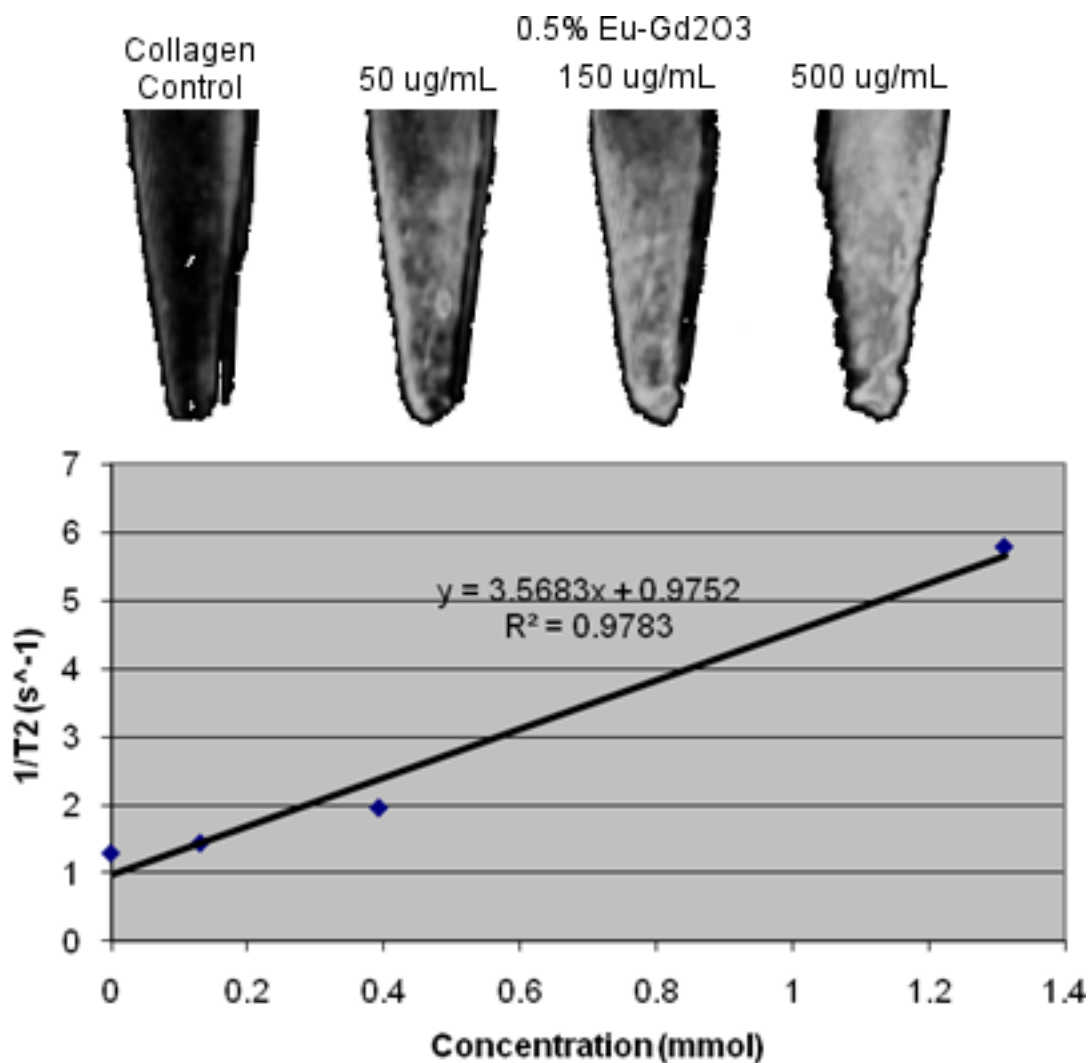


Figure 4. 3-D rendering of the difference subtracted processed MRI of Eppendorf tubes containing the indicated concentrations of nanoparticles suspended in type I collagen.  $r_2$  relaxivities calculated using the described method for various concentrations of gadolinium suspended in collagen and scanned at several echo times ( $T_E = 4, 6, 8, 10, 12, 14, 16, 18,$  and  $20$  ms). The calculated  $T_2$  value was plotted for each nanoparticle concentration and the slope of the best fit line gives the  $r_2$  relaxivity ( $3.6 \text{ s}^{-1} \cdot \text{mM}^{-1}$ ).

A new  $T_2$ -weighted scan at several echo times (4, 6, 8, 10, 12, 14, 16, 18, and 20 ms) was performed so that the  $r_2$  relaxivity value could be calculated and compared with other available particles. Using MATLAB, the original MR images for the tubes were split into individual slices which were reorganized so that each slice contained all the echo times stacked together. One by one, these were processed using the ImageJ plugin “MRI Analysis Calculator” described in the methods section. The calculated  $T_2$  times were reassembled into a single stack so that MIPAV volume-of-interest (VOI) tools could be used to isolate the different concentrations within the scan. The mean  $T_2$  value was calculated for each scan, and a plot of  $1/T_2$  vs. concentration was made (figure 4). The plot shows the equation of the best fit line, used to determine the  $r_2$  relaxivity value for the particles, which was  $3.6 \text{ s}^{-1} \cdot \text{mM}^{-1}$ , and with a strong R-squared value of 0.98.

#### MRI of Fe/FITC-MSN-labeled MSCs

The first *ex vivo* MSN imaging experiments are shown in figure 5. After perfusion fixation of a mouse, the brain and lungs were dissected and injected with a number of Fe/FITC-MSN-labeled stem cells. Injections of 150,000 and 50,000 cells were made into each hemisphere of the brain, and a 50,000 cell injection was made in the lung through the pleura. The organs were stored in 15 mL centrifuge tubes with 4% paraformaldehyde and scanned in the 4.7 Tesla Varian® small animal scanner. After opening the images in MIPAV, each injection site could be observed in the 3-D reconstructions of each organ (figure 5, A and C). The volumes of interest were selected and measurements were made: total volume in voxels and in  $\text{mm}^3$ , and average and standard deviation of the intensity value (in arbitrary units). Control volumes of interest were selected as well from normal tissue away from the injection sites. Statistical comparison of two means was performed on the data, and significance ( $p < 0.05$ ) was observed. In the case of the brain, comparison of the injection site to the nearby ventricles did not show a significant difference.

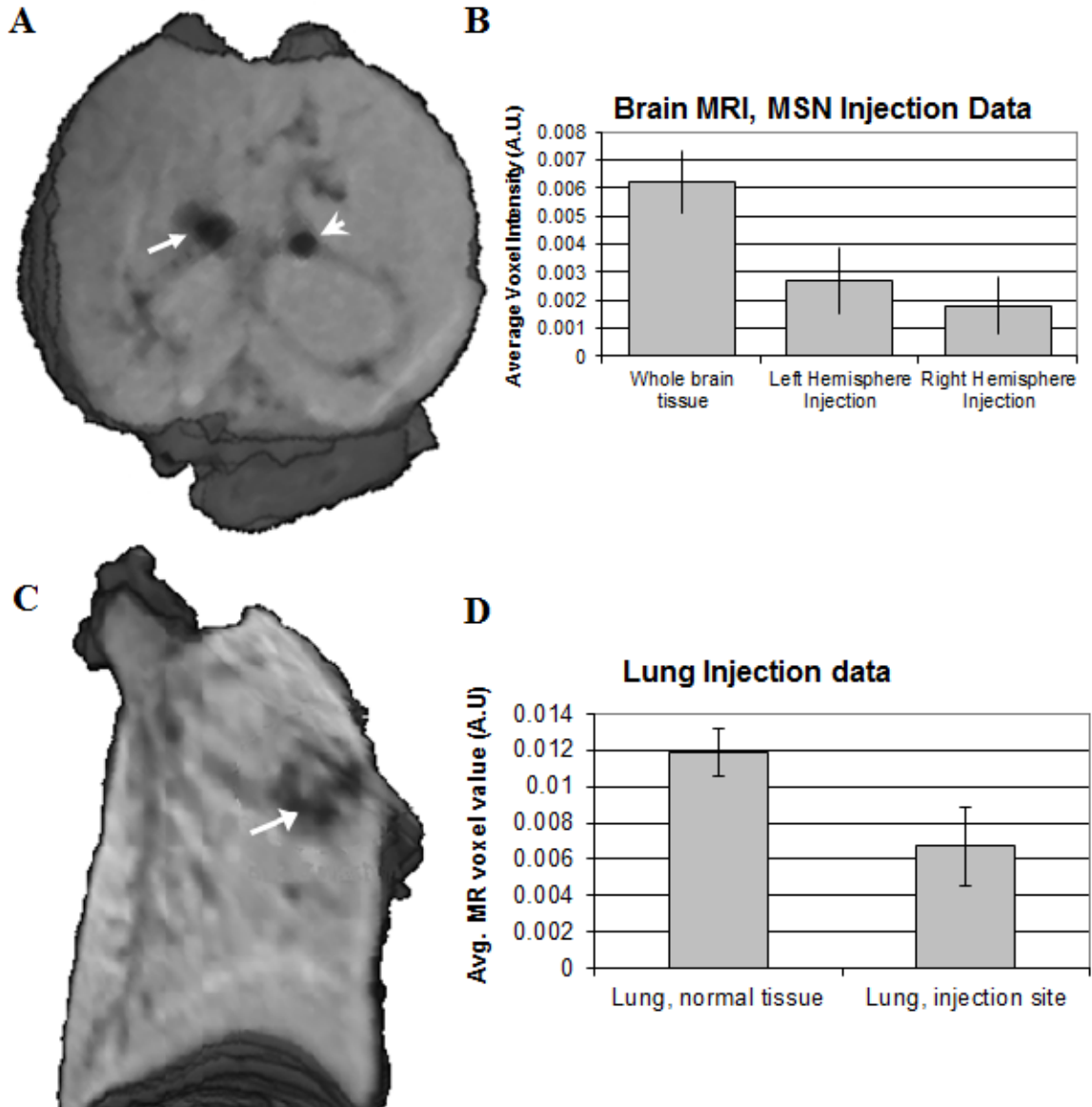


Figure 5. 3D MR rendering of *ex vivo* mouse brain (A) and lung (C), with injection sites highlighted. Brain was injected with 150,000 labeled hMSCs (right hemisphere, arrow head) and 50,000 labeled hMSCs (left hemisphere, arrow). Lung was injected with 50,000 labeled hMSCs (white arrow). Plots of injection sites' values (in arbitrary MR units) compared with normal tissue (B and D). For both plots, error bars indicate the standard deviation of the volume of interest; statistical comparison of normal tissue to injection site gave a value of  $p < 0.05$ .

In the case of the heart, 3 injections of 50,000 cells each were made in the same heart, and their intensity value averaged (figure 6). This average was compared to both normal heart tissue as well as to air bubbles which were trapped in the centrifuge tube, because to the naked eye, these had a similar hypointense value as the injections of cells. In both comparisons, significance was observed.

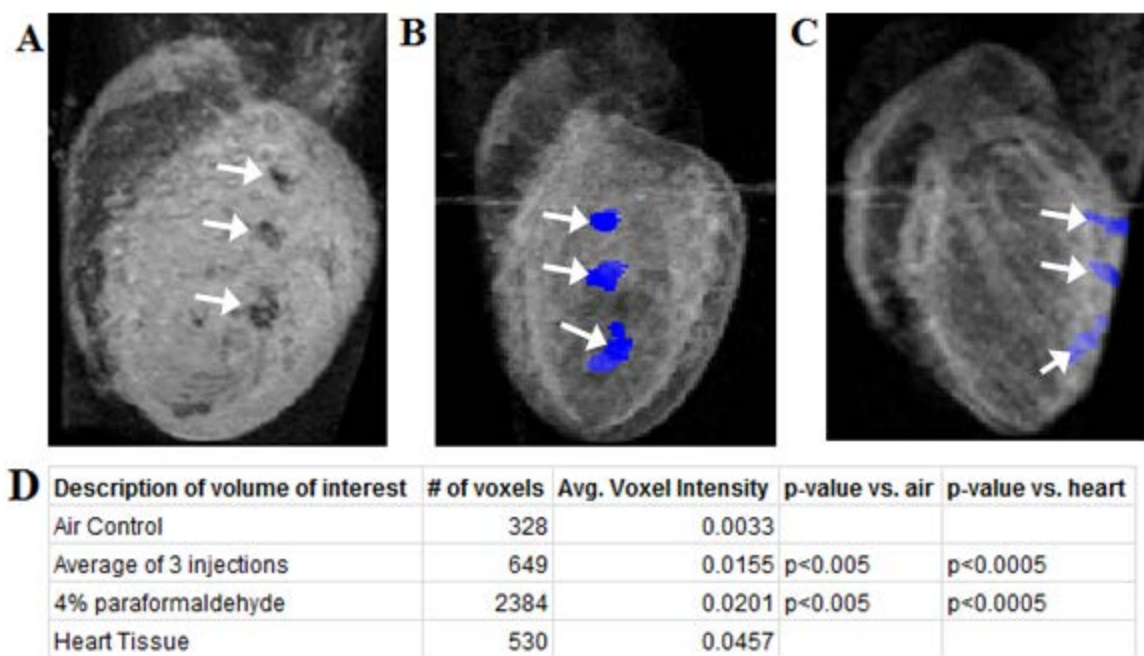


Figure 6. 3D rendering of *ex vivo* mouse heart into which 3 injections of 50,000 labeled hMSCs were added (A). The three injection sites (indicated by arrows) were manually segmented (volumes of interest shown in ventral view, B, and lateral view, C), and statistical analyses performed (D).

### Lung Micro-CT

Compared with MRI where air is avoided, the process for tissue acquisition for CT is more involved because dried tissue gives the best results, yet the lungs cannot be

allowed to deflate. Working with the Hoffman lab, we anesthetized the mouse and performed a tracheotomy to deliver labeled cells followed by constant positive air pressure via the same flexible catheter. With inflation of the lungs maintained, the chest cavity could be opened and the lungs removed and dried for several days in a drying oven, still under positive intratracheal pressure. The process was repeated for cells labeled with gold-, ferrite-, and bismuth-capped MSN particles, and scans were performed with varying source voltages.

The specimen with gold-capped MSN particles scanned at 60 kV provided the best results and is shown in figure 7. In a similar process to the MRI images shown in figures 4 and 5, the volume of interest could be seen and was selected in MIPAV, along with a control volume from the contralateral lung. The volume and CT number information was tabulated for comparison. The difference between the labeled and unlabeled lung could be seen with the naked eye (figure 7B), and despite the high variance present in the lung tissue, statistical significance was achieved ( $p < 0.005$ ).

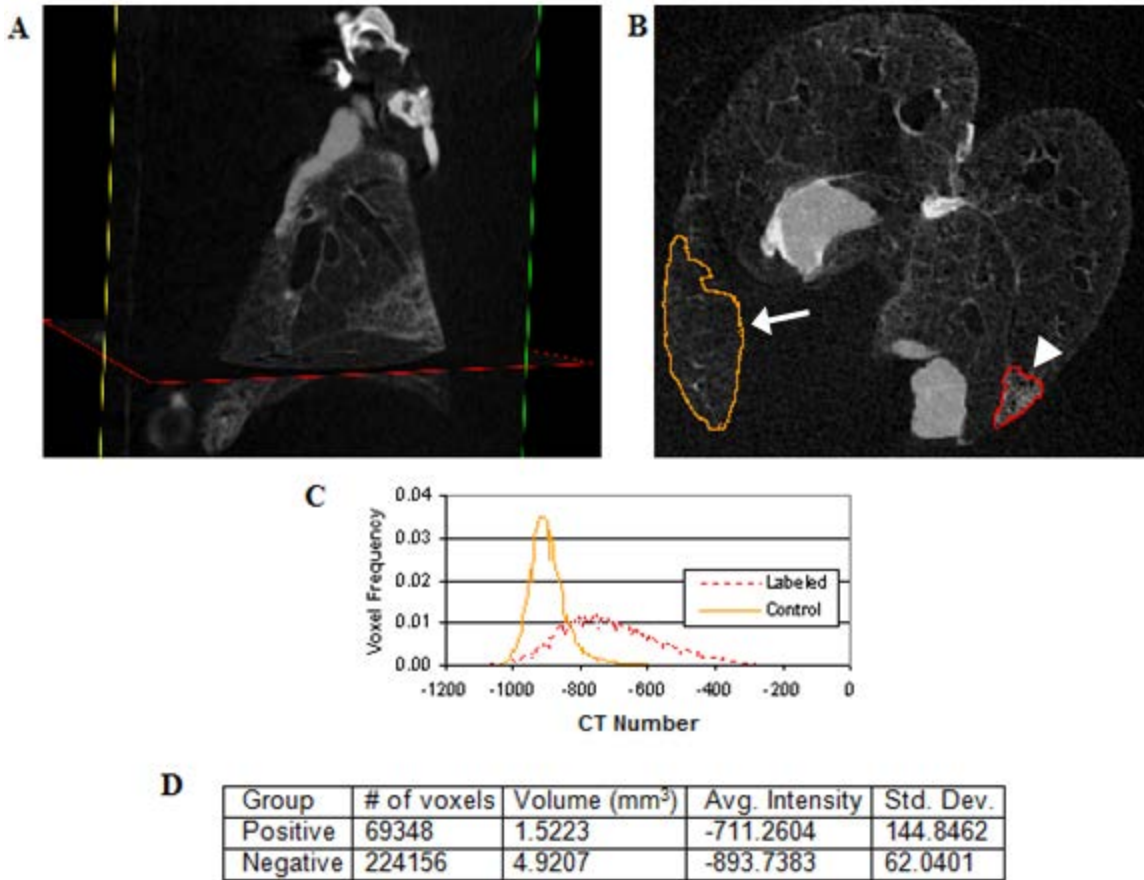


Figure 7: CT of perfusion fixed mouse lung with an intratracheal delivery of  $1.7 \times 10^6$  cells labeled with gold-capped, FITC-loaded MSN particles. Triplanar 3D view (A) shows region of likely labeling superior to slice indicated by red box. In (B), the slice indicated in (A) shows labeled region (arrow head) and unlabeled region (arrow), used for comparison. Histogram (C) comparing profiles of labeled and unlabeled regions corresponding to those shown in (B), with statistical data tabulated in (D).

## CHAPTER IV. DISCUSSION

### MSC Culture Characterization

In order to achieve the ultimate goal of designing a novel *in vivo* stem cell tracking and drug delivery system, the first step was to confirm the potency of our cultured mesenchymal stem cells to form cells of several lineages. Based on published studies, the cell surface marker STRO-1 has the strongest correlation to the cells' differentiability than any other marker. STRO-1 positive cells are capable of differentiating into tissues as varied as adipogenic, chondrogenic, osteogenic, and myocardial.

We isolated mesenchymal stem cells from the greater bone marrow population of human fetal long bones by simply separating adherence-dependent from non-adherence-dependent cells after 1-2 days in culture. Next we used hybridoma-produced monoclonal antibodies to the human STRO-1 marker to confirm expression in the adherent cells. Because immunological staining techniques can be sensitive to non-specific binding and other false positives, it is important to observe not just the presence or absence of signal, but to examine the pattern of expression observed, and compare that using published results as a sort of positive control. In this case, it was observed that STRO-1 was localized in the perinuclear regions of the cell, in a punctiform pattern similar pattern to published data. This expression was observed after 5 days in culture, a time frame suitable for our research at this point. In published data, STRO-1 expression diminishes over about 2 weeks in culture, though it is currently unclear what function STRO-1 serves in the stem cell.

As further confirmation of the potency of our mesenchymal stem cells, we switched our standard growth medium (DMEM/10% fbs) for medium containing growth factors for adipocytes (StemCell Technologies). After 3-5 days in culture, these cells did change morphology to appear as pre-adipocytes. Compared with the elongated, bipolar

morphology of mesenchymal stem cells, pre-adipocytes are more rounded, with several small vacuoles for lipid storage. Mature adipocytes normally have one very large vacuole and stain positive for Oil-Red-O. This observation, along with positive STRO-1 expression, is strong evidence that the cells we have isolated are indeed differentiable stem cells of the bone marrow.

### MSN Particle Kinetics

Following in the success of the previous experiment, we next worked with the lab of Victor S.Y. Lin, Iowa State University, to demonstrate successful uptake of a variety of mesoporous silicate nanoparticles by our stem cells. Much of the previous *in situ* research by the Lin group was performed on HeLa cells. These cells are renowned for being among the first human cells isolated and cultured *in vitro*. On one hand, this makes the choice of these cells a very good one, as this cell line is extremely well-characterized, having been used for decades in many different studies. On the other hand, these are originally cervical cancer cells which divide very rapidly and have been adapted to grow extremely easily on tissue culture surfaces, making them a rather unrealistic model cell to be used for *in vivo* studies. Therefore, we felt demonstrating cellular uptake of MSN particles by our cells was an important key to future experiments.

Initially, the optimal dose of MSN particle was measured. In a 24 well culture plate,  $2.5 \times 10^4$  mesenchymal stem cells were seeded per well, and the MSN doses (in  $\mu\text{g/mL}$ ) were 10, 25, 50, 125, 250, and 500. The maximum dose that did not cause an excessive observable toxicity to the cells was 125  $\mu\text{g/mL}$ . For each new variety of MSN particle we developed with the Lin lab, we repeated this dosage experiment, observing a maximum safe dose of 125  $\mu\text{g/mL}$  each time.

Given that result, each subsequent experiment was performed using 125  $\mu\text{g/mL}$  as a standard dose for all MSN particles. Therefore, we prepared a new culture, using a slightly sparser initial cell population so that it may be observed over a longer time

course. After adding the particles, we observed the cells several times throughout the first day, then daily thereafter. Within hours, the particles could be seen aligning with the cell membranes, and lightly tapping the culture plate showed that the particles did not move from this position. They appeared to be effectively stuck to the cell membranes, rather than loosely associated. The following day, nearly all of the particles were inside the cells, and on subsequent days, the clusters of intracellular particles appeared to decrease in number but increase in size, suggesting the cells are consolidating what they are likely treating as a foreign object. In addition, the majority of the particles seemed to be moved towards the nuclei of the cells as the days progressed.

The uptake mechanism has not been determined with certainty, but in all likelihood is a non-specific form of endocytosis. Because no receptor ligands have been used on these particles, any form of receptor-mediated endocytosis can be ruled out. When labeling mesenchymal stem cells with their MSN particles, Huang et al showed electron micrographic evidence for clathrin-coated pits as the uptake mechanism<sup>91</sup>. In the future, however, the addition of receptor ligands may certainly be an area of interest for delivering these particles to a specific cell *in vivo*.

Additionally, once the particles are endocytosed, the fate of the endosomes is unclear. However, the particles are most likely treated as a foreign object, in which case the particles would be fused with lysosomes in an attempt to destroy them. This has important implications for future experiments if the particles are to be used in drug delivery applications. The acidic environment of a lysosome, with a pH of about 4.5, could be damaging to any reagents before they are able to escape the lysosome.

### Imaging Studies

Gadolinium has gained popularity as an MRI contrast agent because, like iron oxide, it affects large changes in the local magnetic fields where it is present. By virtue of the fact that it has 7 unpaired electrons in its outer shell, it interacts very efficiently

with surrounding protons. If the same specimen is scanned at two different echo times, the changes in field effects between the two scans is larger relative to the differences between background materials. Therefore, a simple subtraction of one image at one echo time from the other further enhances the tracing of the material. Based on the results it seems that europium-doped  $\text{Gd}_2\text{O}_3$  particles that we have developed perform quite well in MRI.

As seen in the graph (figure 4), performing T2 calculations resulted in an  $r_2$  relaxation coefficient of  $3.6 \text{ s}^{-1}\cdot\text{mM}^{-1}$ . By comparison, Regino et al calculated an  $r_2$  coefficient of  $5.44 \text{ s}^{-1}\cdot\text{mM}^{-1}$  for Magnevist® and  $42.08 \text{ s}^{-1}\cdot\text{mM}^{-1}$  for their Gd-G8 dendrimers<sup>65</sup>, while Klasson et al calculated an  $r_2$  of  $4.1 \text{ s}^{-1}\cdot\text{mM}^{-1}$ .<sup>84</sup> While our particles are in the same order of magnitude as similar materials, the relaxivity values seem to be highly dependent on particle size, with smaller particles possessing higher relaxivity values. Our particles did have some problems with agglomeration, so based on the Regino study, the relaxivity may have suffered. Therefore, future efforts to render the particles more monodisperse for improved particle uptake will likely increase the relaxivity.

After completing *in vitro* studies, but before moving to much more difficult and involved *in vivo* studies, we wanted to perform *ex vivo* studies on perfusion fixed organs of mice containing our labeled stem cells to determine the feasibility of our imaging methods. We experimented with imaging of several organs (brain, heart and lungs), using several varieties of MSN particles (iron, gold, and bismuth) and either micro-CT or magnetic resonance imaging.

For micro-CT studies involving the lung, we worked with the lab of Dr. Eric Hoffman on a method for perfusion fixation of the mouse that allowed us to load our particles into the airway tree of the lung without collapsing the delicate lung tissue upon dissection. After performing a tracheotomy, injecting the cells intratracheally, and fixing the lungs under pressure, we observed hyperintense regions in the lung tissue at the most

inferior terminal bronchi of the lung containing labeled stem cells. Measuring the grayscale values of the regions containing labeled stem cells and comparing with normal regions of the contralateral lung, we found a statistically significant change in signal for each of our metallic particles, with the greatest degree of significance in gold particles, which is shown in figure 7.

For MR studies, the method for perfusion fixation was simpler, as we needed all the tissues to remain wet. The mouse was anesthetized, perfusion fixed, and injections were made into the fixed organs, which were removed and scanned while immersed in fixative. Not surprisingly, we did not observe a great deal of contrast using gold and bismuth particles. However, we did observe strong contrast using iron oxide MSN particles in brain, heart and lung. Though the injection sites were clear in the brain, the grey levels of the sites could not be statistically differentiated from the ventricles. This may be in part due to the proximity of the injections to the ventricles. It is likely some of the injected materials diffused into the ventricles altering their intensity. Future experiments involving injections into the mouse brain should be done with more precise equipment, such as a stereotaxic frame.

In the case of both MRI and CT, an important issue that needs to be addressed is the ability to scale-up these results for human testing. The scanners used in these experiments are not clinical, and are designed for small specimens and maximum spatial resolution. The ability to detect labeled cells in these devices does not necessarily reflect the potential to detect them in a human patient with a clinical scanner. However, using some rules of thumb, we can estimate the number of labeled cells we may detect in the scale-up process.

In CT imaging, the signal-to-noise ratio is a function of the number of x-ray photons that reach the detector for each pixel. This is affected by the x-ray source voltage, the properties of the collimator which reduces noise from scattered photons, and the spatial resolution. The source voltage remains the same regardless of whether the

system is a micro-CT or larger clinical CT scanner. The properties of the collimator are unknown, but are assumed to be similar for both scanner types. The biggest difference between the scanner types is the spatial resolution, which can be under 50  $\mu\text{m}$  for micro-CT, and around 0.5 mm for clinical scanners. Therefore, in a worst-case scenario, for a volume of labeled cells to be detected within a voxel that is 10 times larger, the volume should be 10 times larger as well. It is reasonable then to assume that a mass of 17 million cells would be detected in the lungs of a human subject.

In MRI, the signal-to-noise ratio (SNR) is proportional to the magnetic field, the voxel size, and the square root of total scan time. Compared to the above scan parameters, the magnetic field of a clinical scanner is reduced by a factor of 3, the voxel size is increased by a factor of about 2, and the scan time is reduced by as much as 8 times (from up to 4 hours to about a half hour). Therefore, the reduction in signal can be estimated as  $2/(3\sqrt{8})$ , or about 4.2 times smaller. This can be approximately balanced out by increasing the number of labeled cells from the  $5 \cdot 10^4$  that was detected in the above scans to about  $2 \cdot 10^5$ . For both of these estimations, the actual thresholds are likely to vary from these estimates, and for different tissues, and can and should be confirmed through testing of scaled-up phantoms in the clinical scanners at a time when clinical testing is more imminent.

## CHAPTER V. CONCLUSIONS

This Master's thesis is intended to be a summary of the preliminary work done for a larger PhD project in which further development and *in vivo* testing takes place in order to form a completely novel, non-invasive means of tracking stem cell transplants in research or clinical applications. As such, we feel we have established enough background data to warrant proceeding with this project at the next level. Future work will focus in several areas described below. In some of these areas, preliminary work has already begun, but has not been fully evaluated, and was therefore not included in the body of this thesis.

1. Functionalized nanoparticles. Although our materials have been quite successful to this point, they are not specific to a certain cell type, something that will likely be desirable prior to *in vivo* testing. The first step in functionalizing the particles will be coating them in something that makes them more hydrophilic, such as an amino acid. We have already begun work on amino acid-coated gadolinium oxide nanoparticles with the Winterer lab, with some very preliminary results showing promise.

After particles have an outer layer of amino acid, the functionalization is simply binding molecules to that layer. These molecules will likely be proteins, such as growth factors or other transcription factors that signal the stem cell to begin differentiation, or ligands to markers which are present only in a specific cell type. In these cases, a peptide bond may be made between the amino acid coating layer and the protein. Other functionalizing molecules may vary depending on new applications as they arise.

2. Echogenic particles. To this point, very few ultrasound contrast agents are under 100 nm. The spatial resolution achieved in ultrasound is not enough to resolve small materials. In unpublished data using agarose disc phantoms, we have found both the MSN particles and the gadolinium oxide nanoparticles to be echogenic with high resolution 30 MHz ultrasound. In comparison with Definity®, a commercial

echocardiography contrast agent, our particles produce nearly as intense a signal in these phantoms as Definity® at approximately the same concentration. Based on our findings, our collaborating labs are developing new particles specifically for ultrasound which will bind nano-bubbles of high molecular weight gases and should further improve the signal intensity observed.

3. *In vivo* testing. In order to show proof of concept with our particles as tracing stem cells, we have begun the early process of developing mouse models. The first of these is the brain, in which there are many degenerative diseases (Parkinson's, Alzheimer's, stroke, etc.) for which stem cell therapy may be a viable treatment. Tracing injections of these cells and possibly even using these cells to deliver helpful growth factors may be useful as well. In our work on this project, we have performed *in vivo* injections in the brains of two mice, who survived the surgery for 2 and 4 days respectively, at which point they were both sacrificed to perform histology. We have shown we can deliver sufficient particles to the mouse brain so as to be detected in MRI without harm coming to the mouse. Next, we wish to improve the precision of our particle delivery to limit the regions labeled to only a few nuclei. In this manner, we can use post-mortem histological methods to corroborate our MRI findings as they relate to particle movement along known pathways in the brain.

A second area we have planned an *in vivo* model is in the mouse heart. Investigators in the department of cardiology have developed techniques involving ligation of the descending coronary artery to simulate myocardial infarction in mice. Another straightforward test for our cells and particles would be to cause an infarction, then attempt to reduce its size using a mesenchymal stem cell transplant, all while tracking the transplantation using MRI or echocardiography. We have developed techniques for growing primary cultures of cardiomyocytes capable of spontaneous contraction in culture. We plan to study these cells in comparison with mesenchymal stem cells, likely through bioinformatics methods, to possibly identify new factors that

trigger cardiac differentiation in mesenchymal stem cells. It may then be possible to load capped MSN particles with these triggers, implant them in the heart, then trigger the release only when they are *in situ*.

Through these projects pursuant to my PhD dissertation, we hope to show proof-of-concept for our particles as highly customizable materials which can be used for very basic imaging contrast agent applications, or as sophisticated vectors for cell-specific drug delivery or triggers of stem cell growth for researchers performing very specialized experiments. As more stem cell therapies make their way into clinical practice, there may be a market in human applications as well. For these reasons, we feel the novelty and versatility of these materials will make them patentable and ready for commercialization.

## REFERENCES

- (1) Watt, F. M.; Hogan, B. L. Out of Eden: stem cells and their niches. *Science* **2000**, *287*, 1427-1430.
- (2) Odorico, J. S.; Kaufman, D. S.; Thomson, J. A. Multilineage differentiation from human embryonic stem cell lines. *Stem Cells* **2001**, *19*, 193-204.
- (3) Donovan, P. J.; Gearhart, J. The end of the beginning for pluripotent stem cells. *Nature* **2001**, *414*, 92-97.
- (4) Shevchenko, R. V.; James, S. L.; James, S. E. A review of tissue-engineered skin bioconstructs available for skin reconstruction. *J. R. Soc. Interface* **2010**, *7*, 229-258.
- (5) Sakai, D.; Mochida, J.; Yamamoto, Y.; Nomura, T.; Okuma, M.; Nishimura, K.; Nakai, T.; Ando, K.; Hotta, T. Transplantation of mesenchymal stem cells embedded in Atelocollagen gel to the intervertebral disc: a potential therapeutic model for disc degeneration. *Biomaterials* **2003**, *24*, 3531-3541.
- (6) Kuo, C. K.; Li, W. J.; Mauck, R. L.; Tuan, R. S. Cartilage tissue engineering: its potential and uses. *Curr. Opin. Rheumatol.* **2006**, *18*, 64-73.
- (7) Saijo, H.; Chung, U. I.; Igawa, K.; Mori, Y.; Chikazu, D.; Iino, M.; Takato, T. Clinical application of artificial bone in the maxillofacial region. *J. Artif. Organs* **2008**, *11*, 171-176.
- (8) Filova, E.; Straka, F.; Mirejovsky, T.; Masin, J.; Bacakova, L. Tissue-engineered heart valves. *Physiol. Res.* **2009**, *58 Suppl 2*, S141-58.
- (9) Dohmen, P. M.; Konertz, W. Tissue-engineered heart valve scaffolds. *Ann. Thorac. Cardiovasc. Surg.* **2009**, *15*, 362-367.
- (10) Mendelson, K.; Schoen, F. J. Heart valve tissue engineering: concepts, approaches, progress, and challenges. *Ann. Biomed. Eng.* **2006**, *34*, 1799-1819.
- (11) Baccarani, U.; Adani, G. L.; Beltrami, A.; Bresadola, F. State of the art on human hepatocytes: isolation, preservation and clinical use. *Miscellaneous. Current Opinion in Organ Transplantation* **2006**, *11*, 643-647.
- (12) Carpentier, B.; Gautier, A.; Legallais, C. Artificial and bioartificial liver devices: present and future. *Gut* **2009**, *58*, 1690-1702.
- (13) Atala, A. Bioengineered tissues for urogenital repair in children. *Pediatr. Res.* **2008**, *63*, 569-575.

- (14) Fissell, W. H.; Manley, S.; Westover, A.; Humes, H. D.; Fleischman, A. J.; Roy, S. Differentiated growth of human renal tubule cells on thin-film and nanostructured materials. *ASAIO J.* **2006**, *52*, 221-227.
- (15) Lanza, R. P.; Chung, H. Y.; Yoo, J. J.; Wettstein, P. J.; Blackwell, C.; Borson, N.; Hofmeister, E.; Schuch, G.; Soker, S.; Moraes, C. T.; West, M. D.; Atala, A. Generation of histocompatible tissues using nuclear transplantation. *Nat. Biotechnol.* **2002**, *20*, 689-696.
- (16) Prokop, A. Bioartificial pancreas: materials, devices, function, and limitations. *Diabetes Technol. Ther.* **2001**, *3*, 431-449.
- (17) Iwata, H.; Simada, H.; Fukuma, E.; Ibbi, T.; Sato, H. Bioartificial pancreas research in Japan. *Artif. Organs* **2004**, *28*, 45-52.
- (18) Karp, G.; Geer, P. v. d. In *Cell and molecular biology : concepts and experiments / Gerald Karp ; [with] Peter van de*; Wiley: Hoboken, NJ :, 2005; Vol. 4th ed.
- (19) Hynes, R. O. US policies on human embryonic stem cells. *Nat. Rev. Mol. Cell Biol.* **2008**, *9*, 993-997.
- (20) Tanne, J. H. Court allows US human embryonic stem cell research to continue, for now. *BMJ* **2010**, *341*, c5450.
- (21) Lees, J. G.; Lim, S. A.; Croll, T.; Williams, G.; Lui, S.; Cooper-White, J.; McQuade, L. R.; Mathiyalagan, B.; Tuch, B. E. Transplantation of 3D scaffolds seeded with human embryonic stem cells: biological features of surrogate tissue and teratoma-forming potential. *Regen. Med.* **2007**, *2*, 289-300.
- (22) Fong, C. Y.; Gauthaman, K.; Bongso, A. Teratomas from pluripotent stem cells: A clinical hurdle. *J. Cell. Biochem.* **2010**, *111*, 769-781.
- (23) Moore, K. L.; Persaud, T. V. N.; Torchia, M. G. In *The developing human : clinically oriented embryology / Keith L. Moore, T.V.N. Persaud* ; Saunders/Elsevier: Philadelphia, PA :, 2008; Vol. 8th ed.
- (24) Gonzalez, J. L. The legitimization of fetal tissue transplantation research under Roe v. Wade. *Creighton Law. Rev.* **2001**, *34*, 895-925.
- (25) Devine, K. Risky business? The risks and benefits of umbilical cord blood collection. *Med. Law. Rev.* **2010**, *18*, 330-362.
- (26) McDonald, S. J.; Middleton, P. Effect of timing of umbilical cord clamping of term infants on maternal and neonatal outcomes. *Cochrane Database Syst. Rev.* **2008**, (2), CD004074.

- (27) Rabe, H.; Reynolds, G.; Diaz-Rossello, J. Early versus delayed umbilical cord clamping in preterm infants. *Cochrane Database Syst. Rev.* **2004**, (4), CD003248.
- (28) Mukhopadhyay, A.; Madhusudhan, T.; Kumar, R. Hematopoietic stem cells: clinical requirements and developments in ex-vivo culture. *Adv. Biochem. Eng. Biotechnol.* **2004**, 86, 215-253.
- (29) Ahdjoudj, S.; Lasmoles, F.; Oyajobi, B. O.; Lomri, A.; Delannoy, P.; Marie, P. J. Reciprocal control of osteoblast/chondroblast and osteoblast/adipocyte differentiation of multipotential clonal human marrow stromal F/STRO-1(+) cells. *J. Cell. Biochem.* **2001**, 81, 23-38.
- (30) Gronthos, S.; Franklin, D. M.; Leddy, H. A.; Robey, P. G.; Storms, R. W.; Gimble, J. M. Surface protein characterization of human adipose tissue-derived stromal cells. *J. Cell. Physiol.* **2001**, 189, 54-63.
- (31) Psaltis, P. J.; Zannettino, A. C.; Worthley, S. G.; Gronthos, S. Concise review: mesenchymal stromal cells: potential for cardiovascular repair. *Stem Cells* **2008**, 26, 2201-2210.
- (32) D'Ippolito, G.; Diabira, S.; Howard, G. A.; Roos, B. A.; Schiller, P. C. Low oxygen tension inhibits osteogenic differentiation and enhances stemness of human MIAMI cells. *Bone* **2006**, 39, 513-522.
- (33) Yang, X.; Zhang, W.; van den Dolder, J.; Walboomers, X. F.; Bian, Z.; Fan, M.; Jansen, J. A. Multilineage potential of STRO-1+ rat dental pulp cells in vitro. *J. Tissue Eng. Regen. Med.* **2007**, 1, 128-135.
- (34) Simmons, P. J.; Torok-Storb, B. Identification of stromal cell precursors in human bone marrow by a novel monoclonal antibody, STRO-1. *Blood* **1991**, 78, 55-62.
- (35) Simmons, P. J.; Gronthos, S.; Zannettino, A.; Ohta, S.; Graves, S. Isolation, characterization and functional activity of human marrow stromal progenitors in hemopoiesis. *Prog. Clin. Biol. Res.* **1994**, 389, 271-280.
- (36) Gronthos, S.; Graves, S. E.; Ohta, S.; Simmons, P. J. The STRO-1+ fraction of adult human bone marrow contains the osteogenic precursors. *Blood* **1994**, 84, 4164-4173.
- (37) Tamayo, E.; Charbord, P.; Li, J.; Herve, P. A quantitative assay that evaluates the capacity of human stromal cells to support granulomonopoiesis in situ. *Stem Cells* **1994**, 12, 304-315.
- (38) Martens, T. P.; See, F.; Schuster, M. D.; Sondermeijer, H. P.; Hefti, M. M.; Zannettino, A.; Gronthos, S.; Seki, T.; Itescu, S. Mesenchymal lineage precursor cells induce vascular network formation in ischemic myocardium. *Nat. Clin. Pract. Cardiovasc. Med.* **2006**, 3 Suppl 1, S18-22.

- (39) Toma, C.; Pittenger, M. F.; Cahill, K. S.; Byrne, B. J.; Kessler, P. D. Human mesenchymal stem cells differentiate to a cardiomyocyte phenotype in the adult murine heart. *Circulation* **2002**, *105*, 93-98.
- (40) Prockop, D. J.; Gregory, C. A.; Spees, J. L. One strategy for cell and gene therapy: harnessing the power of adult stem cells to repair tissues. *Proc. Natl. Acad. Sci. U. S. A.* **2003**, *100 Suppl 1*, 11917-11923.
- (41) Studeny, M.; Marini, F. C.; Dembinski, J. L.; Zompetta, C.; Cabreira-Hansen, M.; Bekele, B. N.; Champlin, R. E.; Andreeff, M. Mesenchymal stem cells: potential precursors for tumor stroma and targeted-delivery vehicles for anticancer agents. *J. Natl. Cancer Inst.* **2004**, *96*, 1593-1603.
- (42) Valiunas, V.; Doronin, S.; Valiuniene, L.; Potapova, I.; Zuckerman, J.; Walcott, B.; Robinson, R. B.; Rosen, M. R.; Brink, P. R.; Cohen, I. S. Human mesenchymal stem cells make cardiac connexins and form functional gap junctions. *J. Physiol.* **2004**, *555*, 617-626.
- (43) Delorme, B.; Chateauvieux, S.; Charbord, P. The concept of mesenchymal stem cells. *Regen. Med.* **2006**, *1*, 497-509.
- (44) Simmons, P. J.; Torok-Storb, B. CD34 expression by stromal precursors in normal human adult bone marrow. *Blood* **1991**, *78*, 2848-2853.
- (45) Garcia-Pacheco, J. M.; Oliver, C.; Kimatrai, M.; Blanco, F. J.; Olivares, E. G. Human decidual stromal cells express CD34 and STRO-1 and are related to bone marrow stromal precursors. *Mol. Hum. Reprod.* **2001**, *7*, 1151-1157.
- (46) Letchford, J.; Cardwell, A. M.; Stewart, K.; Coogans, K. K.; Cox, J. P.; Lee, M.; Beresford, J. N.; Perry, M. J.; Welham, M. J. Isolation of C15: a novel antibody generated by phage display against mesenchymal stem cell-enriched fractions of adult human marrow. *J. Immunol. Methods* **2006**, *308*, 124-137.
- (47) Stewart, K.; Monk, P.; Walsh, S.; Jefferiss, C. M.; Letchford, J.; Beresford, J. N. STRO-1, HOP-26 (CD63), CD49a and SB-10 (CD166) as markers of primitive human marrow stromal cells and their more differentiated progeny: a comparative investigation in vitro. *Cell Tissue Res.* **2003**, *313*, 281-290.
- (48) Galmiche, M. C.; Koteliansky, V. E.; Briere, J.; Herve, P.; Charbord, P. Stromal cells from human long-term marrow cultures are mesenchymal cells that differentiate following a vascular smooth muscle differentiation pathway. *Blood* **1993**, *82*, 66-76.
- (49) Baddoo, M.; Hill, K.; Wilkinson, R.; Gaupp, D.; Hughes, C.; Kopen, G. C.; Phinney, D. G. Characterization of mesenchymal stem cells isolated from murine bone marrow by negative selection. *J. Cell. Biochem.* **2003**, *89*, 1235-1249.

- (50) Frank, J. A.; Miller, B. R.; Arbab, A. S.; Zywicke, H. A.; Jordan, E. K.; Lewis, B. K.; Bryant, L. H., Jr; Bulte, J. W. Clinically applicable labeling of mammalian and stem cells by combining superparamagnetic iron oxides and transfection agents. *Radiology* **2003**, *228*, 480-487.
- (51) Bos, C.; Delmas, Y.; Desmouliere, A.; Solanilla, A.; Hauger, O.; Grosset, C.; Dubus, I.; Ivanovic, Z.; Rosenbaum, J.; Charbord, P.; Combe, C.; Bulte, J. W.; Moonen, C. T.; Ripoche, J.; Grenier, N. In vivo MR imaging of intravascularly injected magnetically labeled mesenchymal stem cells in rat kidney and liver. *Radiology* **2004**, *233*, 781-789.
- (52) Ju, S.; Teng, G.; Zhang, Y.; Ma, M.; Chen, F.; Ni, Y. In vitro labeling and MRI of mesenchymal stem cells from human umbilical cord blood. *Magn. Reson. Imaging* **2006**, *24*, 611-617.
- (53) Peldschus, K.; Kaul, M.; Lange, C.; Nolte-Ernsting, C.; Adam, G.; Ittrich, H. Magnetic resonance imaging of single SPIO labeled mesenchymal stem cells at 3 Tesla. *Rofo* **2007**, *179*, 473-479.
- (54) Winkler, T.; von Roth, P.; Schuman, M. R.; Sieland, K.; Stoltenburg-Didinger, G.; Taupitz, M.; Perka, C.; Duda, G. N.; Matziolis, G. In vivo visualization of locally transplanted mesenchymal stem cells in the severely injured muscle in rats. *Tissue Eng. Part A*. **2008**, *14*, 1149-1160.
- (55) Gregory, C. A.; Singh, H.; Perry, A. S.; Prockop, D. J. The Wnt signaling inhibitor dickkopf-1 is required for reentry into the cell cycle of human adult stem cells from bone marrow. *J. Biol. Chem.* **2003**, *278*, 28067-28078.
- (56) Gregory, C. A.; Perry, A. S.; Reyes, E.; Conley, A.; Gunn, W. G.; Prockop, D. J. Dkk-1-derived synthetic peptides and lithium chloride for the control and recovery of adult stem cells from bone marrow. *J. Biol. Chem.* **2005**, *280*, 2309-2323.
- (57) Gunn, W. G.; Conley, A.; Deininger, L.; Olson, S. D.; Prockop, D. J.; Gregory, C. A. A crosstalk between myeloma cells and marrow stromal cells stimulates production of DKK1 and interleukin-6: a potential role in the development of lytic bone disease and tumor progression in multiple myeloma. *Stem Cells* **2006**, *24*, 986-991.
- (58) Slowing, I.; Trewyn, B. G.; Lin, V. S. Effect of surface functionalization of MCM-41-type mesoporous silica nanoparticles on the endocytosis by human cancer cells. *J. Am. Chem. Soc.* **2006**, *128*, 14792-14793.
- (59) Slowing, I. I.; Trewyn, B. G.; Lin, V. S. Mesoporous silica nanoparticles for intracellular delivery of membrane-impermeable proteins. *J. Am. Chem. Soc.* **2007**, *129*, 8845-8849.

- (60) Lai, C. Y.; Trewyn, B. G.; Jęftinija, D. M.; Jęftinija, K.; Xu, S.; Jęftinija, S.; Lin, V. S. A mesoporous silica nanosphere-based carrier system with chemically removable CdS nanoparticle caps for stimuli-responsive controlled release of neurotransmitters and drug molecules. *J. Am. Chem. Soc.* **2003**, *125*, 4451-4459.
- (61) Shellock, F. G.; Kanal, E. Safety of magnetic resonance imaging contrast agents. *J. Magn. Reson. Imaging* **1999**, *10*, 477-484.
- (62) Cheong, B. Y.; Muthupillai, R. Nephrogenic systemic fibrosis: a concise review for cardiologists. *Tex. Heart Inst. J.* **2010**, *37*, 508-515.
- (63) Kobayashi, H.; Brechbiel, M. W. Nano-sized MRI contrast agents with dendrimer cores. *Adv. Drug Deliv. Rev.* **2005**, *57*, 2271-2286.
- (64) Debbage, P.; Jaschke, W. Molecular imaging with nanoparticles: giant roles for dwarf actors. *Histochem. Cell Biol.* **2008**, *130*, 845-875.
- (65) Regino, C. A.; Walbridge, S.; Bernardo, M.; Wong, K. J.; Johnson, D.; Lonser, R.; Oldfield, E. H.; Choyke, P. L.; Brechbiel, M. W. A dual CT-MR dendrimer contrast agent as a surrogate marker for convection-enhanced delivery of intracerebral macromolecular therapeutic agents. *Contrast Media Mol. Imaging* **2008**, *3*, 2-8.
- (66) Caravan, P.; Ellison, J. J.; McMurry, T. J.; Lauffer, R. B. Gadolinium(III) Chelates as MRI Contrast Agents: Structure, Dynamics, and Applications. *Chem. Rev.* **1999**, *99*, 2293-2352.
- (67) Park, J. Y.; Baek, M. J.; Choi, E. S.; Woo, S.; Kim, J. H.; Kim, T. J.; Jung, J. C.; Chae, K. S.; Chang, Y.; Lee, G. H. Paramagnetic ultrasmall gadolinium oxide nanoparticles as advanced T1 MRI contrast agent: account for large longitudinal relaxivity, optimal particle diameter, and in vivo T1 MR images. *ACS Nano* **2009**, *3*, 3663-3669.
- (68) Crich, S. G.; Biancone, L.; Cantaluppi, V.; Duo, D.; Esposito, G.; Russo, S.; Camussi, G.; Aime, S. Improved route for the visualization of stem cells labeled with a Gd-/Eu-chelate as dual (MRI and fluorescence) agent. *Magn. Reson. Med.* **2004**, *51*, 938-944.
- (69) Park, Y. I.; Kim, J. H.; Lee, K. T.; Jeon, K.; Na, H. B.; Yu, J. H.; Kim, H. M.; Lee, N.; Choi, S. H.; Baik, S.; Kim, H.; Park, S. P.; Park, B.; Kim, Y. W.; Lee, S. H.; Yoon, S.; Song, I. C.; Moon, W. K.; Suh, Y. D.; Hyeon, T. Nonblinking and Nonbleaching Upconverting Nanoparticles as an Optical Imaging Nanoprobe and T1 Magnetic Resonance Imaging Contrast Agent. *Adv Mater* **2009**, *21*, 4467-4471.
- (70) Werts, M. H. Making sense of lanthanide luminescence. *Sci. Prog.* **2005**, *88*, 101-131.

- (71) Groman, E. V.; Bouchard, J. C.; Reinhardt, C. P.; Vaccaro, D. E. Ultrasmall mixed ferrite colloids as multidimensional magnetic resonance imaging, cell labeling, and cell sorting agents. *Bioconjug. Chem.* **2007**, *18*, 1763-1771.
- (72) Goldys, E. M.; Drozdowicz-Tomsia, K.; Jinjun, S.; Dosev, D.; Kennedy, I. M.; Yatsunenko, S.; Godlewski, M. Optical characterization of eu-doped and undoped  $\text{gd}(2)\text{o}(3)$  nanoparticles synthesized by the hydrogen flame pyrolysis method. *J. Am. Chem. Soc.* **2006**, *128*, 14498-14505.
- (73) Liang, Z.; Lauterbur, P. C.; IEEE Engineering in Medicine and Biology Society In *Principles of magnetic resonance imaging : a signal processing perspective / Zhi-Pei Lian*; SPIE Optical Engineering Press ; IEEE Press: Bellingham, Wash. : New York, NY:., 2000; .
- (74) Lauffer, R. B. Paramagnetic metal complexes as water proton relaxation agents for NMR imaging: theory and design. *Chem. Rev.* **1987**, *87*, 901-927.
- (75) Webster, J. G.; Clark, J. W. In *Medical instrumentation : application and design / John G. Webster, editor ; contributing*; Wiley: New York :, 1998; Vol. 3rd ed.
- (76) Yu, S. B.; Watson, A. D. Metal-Based X-ray Contrast Media. *Chem. Rev.* **1999**, *99*, 2353-2378.
- (77) Hoehn, M.; Kustermann, E.; Blunk, J.; Wiedermann, D.; Trapp, T.; Wecker, S.; Focking, M.; Arnold, H.; Hescheler, J.; Fleischmann, B. K.; Schwindt, W.; Buehrle, C. Monitoring of implanted stem cell migration in vivo: a highly resolved in vivo magnetic resonance imaging investigation of experimental stroke in rat. *Proc. Natl. Acad. Sci. U. S. A.* **2002**, *99*, 16267-16272.
- (78) Kustermann, E.; Roell, W.; Breitbach, M.; Wecker, S.; Wiedermann, D.; Buehrle, C.; Welz, A.; Hescheler, J.; Fleischmann, B. K.; Hoehn, M. Stem cell implantation in ischemic mouse heart: a high-resolution magnetic resonance imaging investigation. *NMR Biomed.* **2005**, *18*, 362-370.
- (79) Daldrup-Link, H. E.; Rudelius, M.; Oostendorp, R. A.; Settles, M.; Piontek, G.; Metz, S.; Rosenbrock, H.; Keller, U.; Heinzmann, U.; Rummeny, E. J.; Schlegel, J.; Link, T. M. Targeting of hematopoietic progenitor cells with MR contrast agents. *Radiology* **2003**, *228*, 760-767.
- (80) Daldrup-Link, H. E.; Rudelius, M.; Piontek, G.; Metz, S.; Brauer, R.; Debus, G.; Corot, C.; Schlegel, J.; Link, T. M.; Peschel, C.; Rummeny, E. J.; Oostendorp, R. A. Migration of iron oxide-labeled human hematopoietic progenitor cells in a mouse model: in vivo monitoring with 1.5-T MR imaging equipment. *Radiology* **2005**, *234*, 197-205.

- (81) Jendelova, P.; Herynek, V.; Urdzikova, L.; Glogarova, K.; Kroupova, J.; Andersson, B.; Bryja, V.; Burian, M.; Hajek, M.; Sykova, E. Magnetic resonance tracking of transplanted bone marrow and embryonic stem cells labeled by iron oxide nanoparticles in rat brain and spinal cord. *J. Neurosci. Res.* **2004**, *76*, 232-243.
- (82) Ko, I. K.; Song, H. T.; Cho, E. J.; Lee, E. S.; Huh, Y. M.; Suh, J. S. In vivo MR imaging of tissue-engineered human mesenchymal stem cells transplanted to mouse: a preliminary study. *Ann. Biomed. Eng.* **2007**, *35*, 101-108.
- (83) Hsiao, J. K.; Tsai, C. P.; Chung, T. H.; Hung, Y.; Yao, M.; Liu, H. M.; Mou, C. Y.; Yang, C. S.; Chen, Y. C.; Huang, D. M. Mesoporous silica nanoparticles as a delivery system of gadolinium for effective human stem cell tracking. *Small* **2008**, *4*, 1445-1452.
- (84) Klasson, A.; Ahren, M.; Hellqvist, E.; Soderlind, F.; Rosen, A.; Kall, P. O.; Uvdal, K.; Engstrom, M. Positive MRI contrast enhancement in THP-1 cells with Gd<sub>2</sub>O<sub>3</sub> nanoparticles. *Contrast Media Mol. Imaging* **2008**, *3*, 106-111.
- (85) Galperin, A.; Margel, S. Synthesis and characterization of radiopaque magnetic core-shell nanoparticles for X-ray imaging applications. *J. Biomed. Mater. Res. B. Appl. Biomater.* **2007**, *83*, 490-498.
- (86) Hainfeld, J. F.; Slatkin, D. N.; Focella, T. M.; Smilowitz, H. M. Gold nanoparticles: a new X-ray contrast agent. *Br. J. Radiol.* **2006**, *79*, 248-253.
- (87) Rabin, O.; Manuel Perez, J.; Grimm, J.; Wojtkiewicz, G.; Weissleder, R. An X-ray computed tomography imaging agent based on long-circulating bismuth sulphide nanoparticles. *Nat. Mater.* **2006**, *5*, 118-122.
- (88) Cormode, D. P.; Skajaa, T.; van Schooneveld, M. M.; Koole, R.; Jarzyna, P.; Lobatto, M. E.; Calcagno, C.; Barazza, A.; Gordon, R. E.; Zanzonico, P.; Fisher, E. A.; Fayad, Z. A.; Mulder, W. J. Nanocrystal core high-density lipoproteins: a multimodality contrast agent platform. *Nano Lett.* **2008**, *8*, 3715-3723.
- (89) Pountos, I.; Corscadden, D.; Emery, P.; Giannoudis, P. V. Mesenchymal stem cell tissue engineering: techniques for isolation, expansion and application. *Injury* **2007**, *38 Suppl 4*, S23-33.
- (90) Sun, Y.; Mulkern, R. V.; Schmidt, K.; Doshi, S.; Albert, M. S.; Schmidt, N. O.; Ziu, M.; Black, P.; Carrol, R.; Kieran, M. W. Quantification of water diffusion and relaxation times of human U87 tumors in a mouse model. *NMR Biomed.* **2004**, *17*, 399-404.
- (91) Huang, D. M.; Hung, Y.; Ko, B. S.; Hsu, S. C.; Chen, W. H.; Chien, C. L.; Tsai, C. P.; Kuo, C. T.; Kang, J. C.; Yang, C. S.; Mou, C. Y.; Chen, Y. C. Highly efficient

cellular labeling of mesoporous nanoparticles in human mesenchymal stem cells: implication for stem cell tracking. *FASEB J.* **2005**, *19*, 2014-2016.